Analysis of 3D linear elastic masonry–like structures through the API of a finite element software

Deborah Briccola

Department of Civil and Environmental Engineering, Politecnico di Milano, I20133, Milano, Italy

Matteo Bruggi[1,]

Department of Civil and Environmental Engineering, Politecnico di Milano, I20133, Milano, Italy

Abstract

A new numerical procedure is presented to perform the analysis of three–dimensional linear elastic no–tension structures exploiting the application programming interface of a general purpose finite element analysis software. Masonry is replaced by an equivalent orthotropic material with spatially varying elastic properties and negligible stiffness in the case of cracking strain. A non–incremental algorithm is implemented to define the distribution of the equivalent material, minimizing the strain energy so as to achieve a compression–only state of stress for any given compatible load. Applications are shown for masonry–like solids of general shape visualizing load paths in walls subject to dead loads and out–of–plane live loads, circular domes under self–weight and a groin vault acted upon by both vertical and horizontal seismic loading.

Keywords: energy–based methods, linear elastic no–tension material, historical masonry structures, masonry domes, masonry vaults, masonry walls.

Email addresses: deborah.briccola@polimi.it (Deborah Briccola), matteo.bruggi@polimi.it (Matteo Bruggi)

1. Introduction

Masonry, whether of bricks or stones, is well known to be a material with low tensile strength. The inability of transferring significant tensile stresses explains the extensive crack patterns that can frequently be observed in ancient masonry construction. However, cracks are not necessarily symptomatic of a possible failure, since stresses can spontaneously attain a purely compressive state, which means that cracked regions do not necessary result in instability of the building. The brittle behavior in tension is one of the main reasons for the high non–linearity of the mechanical response of masonry structures. Numerous micro– and macro– models, with different degree of complexity and sophistication, have been developed over the years to properly address this issue both from a constitutive and a numerical point of view, see e.g. [46] for a comprehensive review and [48] for recent trends.

To mention a few, discontinuous idealizations based on the representation of masonry as a continuous medium cut by joints [33] belong to the former class of models. The first numerical implementation of such an approach in 3D was presented in [19]. These models have proved to be reliable in the interpretation of experimental test results and damage observed on site [32], although the computational cost can be a challenge in the application to complex structures. Other micro–models that include damage laws and assume progressive micro–cracking and strength–loss have been proposed as equivalent continuum idealizations, see e.g. [34, 8, 45]. Several model parameters are needed to achieve an as-much-as-possible realistic mechanical response. Unfortunately, extended experimental data is not easily available for historical masonry construction [35]. Moreover, complex non–linear finite element procedures are generally needed to handle such kind of models. To overcome this issue, the contribution in [38] proposes an effective and accurate computational strategy for brick masonry structures that adopts a domain partitioning approach coupled with a meso–scale finite element model, see also [42, 15].

Considering the above aspects, a continuum idealization endowed with the *linear elastic masonry–*

like material model can be seen as a meaningful mechanical approximation when dealing with the preliminary assessment of historical masonry construction, see e.g. [17]. It assumes (i) the stress tensor to be negative semi–definite (unilateral constraint), (ii) the strain to be the sum of an elastic and inelastic part (small displacements and strains are considered), (iii) the negative semi–definite stress tensor to be linearly dependent upon the elastic part of the strain and (iv) the positive semi–definite inelastic strain to be normal to the stress tensor, see in particular [22].

Despite the apparent simplicity of the above assumptions, specific issues arise such as the need for compatibility of the external loads with respect to the no–tension constraint, the non–uniqueness of the solution due to the inelastic (cracking) strains and the discontinuities that are likely to affect both the stress and the displacement field, see [3].

As reviewed in [20], there are different numerical methods to cope with the linear elastic masonry–like material model, including total displacement formulations or displacement rate approaches, see e.g. [47, 25, 36, 1], as well as stress (complementary) formulations, see e.g. [40, 26, 20]. Reference is also made to the contribution in [41], which proposes a generalization of the classical model to account for irreversible crushing strains. While most of the above formulations have been implemented and tested for in–plane problems, the work in [37] adopts non conforming shell elements to search for thrust surfaces in linear elastic no–tension masonry vaults through appropriate nonlinear techniques.

Alternatively, the no–tension assumption can be handled robustly through energy–based minimization procedures, as discussed e.g. in [6]. A numerical method was proposed in [4] that solves the equilibrium of two–dimensional no–tension bodies seeking for the displacement field that minimizes a suitable form of the total potential energy adopting the displacement field as unknown.

Within this framework, the real masonry–like body can be replaced by an equivalent orthotropic medium to mimic the strain energy contributions of the no–tension material by enforcing a neg-

ligible stiffness in any direction along which a tensile strain arises [12]. For any given load that is compatible with the no–tension assumption, the equilibrium of the body is sought by minimizing the strain energy with respect to the distribution of the equivalent orthotropic material. This requires the iterative computation of the displacement and stress fields depending on the current values of a set of minimization parameters. The arising minimization problem was solved in [13] through sequential convex programming, with the aim of investigating the in–plane and out–of–plane behavior of masonry walls and arches by means of two–dimensional models. A preliminary extension to the three–dimensional framework has recently been explored in [11], where regular meshes of eight–node hexahedral elements are dealt with on simple geometries. As a straightforward generalization of the two–dimensional approach, mathematical programming was implemented to cope with the minimization procedure, whereas the orientation of the orthotropic medium with respect to the global reference system was handled using Euler's angles. Notwithstanding the simplicity of the discretizations, which were all based on the repetition of the same cubic element, a bottle–neck related to the computation of the objective function and its sensitivity was reported. This was also tied to a certain complexity in the handling of the orientation of the symmetry planes of the equivalent orthotropic material when dealing with the element stiffness matrices and their derivatives.

This contribution presents an efficient numerical approach to analyze 3D linear elastic masonry–like bodies exploiting: (i) the application programming interface (API) of any general purpose software package performing the finite element analysis (FEA) of linear elastic orthotropic media and (ii) an efficient scheme to update the minimization parameters based on a penalized steepest descent–like method.

The proposed approach is ideally conceived to visualize load paths in structural components of historical masonry buildings, such as walls, vaults and domes, when subjected to any compatible set of dead loads and live loads. Indeed, the linear elastic no–tension model requires the definition

of a limited number of constitutive parameters, the adoption of an energy–based approach avoids the need for non–linear approaches, and the implementation within a finite element package allows general shapes to be handled and the exploitation of efficient sparse linear solvers. Basic matrix operations on the principal stresses and on the relevant direction cosines are performed to update the constitutive properties of the equivalent orthotropic material throughout the finite element discretization. These quantities, as well as the overall strain energy, are directly computed by the post–processing routines of the finite element software package.

The proposed approach may also be used to investigate the structural behavior of masonry–like structures at failure. Mechanisms and collapse load multipliers are found without any *a–priori* hypothesis on the failure mode, as conversely needed when assuming a rigid–plastic material model in classical limit analysis, see the well–known *rigid no–tension material* model in [28].

It is finally remarked that the assumptions governing the linear elastic no–tension material model imply limitations that need to be considered when addressing the analysis of historical constructions under monotonic loading. In particular, inelastic strains are assumed to be normal to the compressive stress tensor, meaning that friction between the voussoirs must be sufficient to prevent sliding failure of one voussoir relative to its neighbours. Positive semi–definite strains arise to recover kinematic. They allow detecting regions where cracks can appear, but they do not provide any information to recover crack patterns or crack widths. No crushing collapse can be modeled, although the evaluation of compressive stresses throughout the structure allows assessing safety through the permissible stress design approach.

The layout of the paper is as follows. The mathematical formulation governing the equilibrium of linear elastic masonry–like bodies is recalled in Section 2.1. The three–dimensional energy function and the constitutive law for the equivalent orthotropic composite are derived in Section 2.2 and Section 2.3, respectively. The adopted energy–based approach is outlined in Section 3.1, whereas its implementation using the API of a finite element software package is detailed in Sections

3.2 and 3.3. Section 4 addresses numerical simulations, e.g. walls with openings subject to dead loads and out–of–plane live loads, circular domes under self–weight and a groin vault under both vertical and horizontal seismic loading. Finally, the main results of the work described in this paper are summarized and on–going developments are outlined in Section 5.

2. Governing equations

2.1. Linear elastic masonry–like materials

According to [22], the so–called *linear elastic masonry–like material* is defined by the following statements:

$$\sigma_{ij} \in Sym^{-}, \tag{1a}$$

$$\varepsilon_{ij} = \varepsilon^{e}_{ij} + \varepsilon^{c}_{ij}, \tag{1b}$$

$$\sigma_{ij} = C_{ijhk}\varepsilon^{e}_{hk}, \tag{1c}$$

$$\sigma_{ij}\varepsilon^{c}_{ij} = 0, \quad \text{and} \quad \varepsilon^{c}_{ij} \in Sym^{+}. \tag{1d}$$

Eqn. (1a) forces the stress σ_{ij} to belong to the closed cone of negative semi–definite symmetric second order tensors Sym^{-}. This constraint is equivalent to preventing the principal stresses from being positive, see e.g. [47]:

$$\begin{aligned} &\sigma_{11} \leq 0, \quad \sigma_{22} \leq 0, \quad \sigma_{33} \leq 0, \quad \det(\underline{\underline{\sigma}}) \leq 0 \\ &\sigma_{22}\sigma_{33} - \sigma^{2}_{23} \geq 0, \quad \sigma_{11}\sigma_{33} - \sigma^{2}_{13} \geq 0, \quad \sigma_{11}\sigma_{22} - \sigma^{2}_{12} \geq 0. \end{aligned} \tag{2}$$

The infinitesimal strain tensor is defined as $\varepsilon_{ij} = \frac{1}{2}(u_{i,j} + u_{j,i})$, where $\underline{u}$ is the displacement field. According to Eqn. (1b), the tensor ε_{ij} is assumed to be the sum of an elastic part ε^{e}_{ij} and a latent one ε^{c}_{ij} accounting for "cracking strains". The elastic part of the strain tensor is related to the stress through the linear relationship in Eqn. (1c), whereas the hypothesis of normality holds for

the latent part of the strain tensor ε^c_{ij}, being Sym^+ in Eqn. (1d) the closed cone of positive semi–definite symmetric second order tensors. This calls for inelastic strains (herein "cracking strains") that can only arise orthogonally to the non–positive stress σ_{ij}, similarly to standard associated plasticity.

2.2. A strain energy function for three–dimensional no–tension elastic problems

Any linear elastic masonry–like material with symmetric elastic tensor C_{ijhk} is hyper–elastic and therefore admits a strain energy density function $\phi(\underline{\underline{\varepsilon}}^e)$. The case of isotropic linear elastic masonry–like materials whose elastic behavior is fully described by the Young's modulus E and the Poisson's ratio $\nu > 0$ is herein dealt with in a general three–dimensional framework.

Let σ_α, $\alpha = I, II, III$, be the eigenvalues of the stress tensor $\underline{\underline{\sigma}}(\chi)$ computed at any point $\chi \in \Omega$, with $\sigma_I \leq \sigma_{II} \leq \sigma_{III}$. z_α, $= \alpha = I, II, III$, are the corresponding eigenvectors.

Following [47], the behavior of the no–tension solid may be conveniently investigated by dividing Ω into four subdomains such that $\Omega = \Omega_1 \cup \Omega_2 \cup \Omega_3 \cup \Omega_4$ and:

$$\begin{aligned}
&\Omega_1 = \chi \in \Omega : \sigma_I < 0,\ \sigma_{II} < 0,\ \sigma_{III} < 0,\\
&\Omega_2 = \chi \in \Omega : \sigma_I < 0,\ \sigma_{II} < 0,\ \sigma_{III} = 0,\\
&\Omega_3 = \chi \in \Omega : \sigma_I < 0,\ \sigma_{II} = 0,\\
&\Omega_4 = \chi \in \Omega : \sigma_I = 0.
\end{aligned} \tag{3}$$

In subdomain Ω_1 the material is subjected to triaxial compression and behaves like a conventional intact isotropic solid. In fact, due to Eqns. (1d) no latent strain is allowed, that is $\varepsilon^c_{ij} = 0$, and the total strain fully turns into the elastic strain $\varepsilon_{ij} = \varepsilon^e_{ij}$. In Ω_2 the material is subjected to biaxial compression and behaves like a transversally isotropic material with axis z_{III}. Indeed, some "cracking strain" $\varepsilon^c \geq 0$ is allowed in the direction orthogonal to the plane $z_I\ z_{II}$, whereas a fully elastic behavior is found in this plane. In Ω_3 the material is subjected to uniaxial compression

and behaves like a transversally isotropic material with axis z_I. According to Eqn. (1d) the material is intact along this axis, whereas "cracking strains" $\varepsilon^c \geq 0$ are allowed in the orthogonal plane $z_{II}\ z_{III}$. Finally, in subdomain Ω_4 neither stress nor elastic strain is found and the material behaves like a "void phase", allowing for any positive semi–definite "cracking strain" to restore compatibility.

Due to the linear elastic behavior in compression and the normality condition, stresses and total strains share the same principal directions. Hence, by exploiting Eqn. (1c) and expressing the generalized Hooke's law in terms of the principal directions, the strain energy function for a 3D linear elastic masonry–like material may straightforwardly be written in terms of the total strain tensor eigenvalues ε_α, $\alpha = I, II, III$, as:

$$\phi(\underline{\underline{\varepsilon}}) = \begin{cases} \dfrac{E}{2(1+\nu)(1-2\nu)}\Big[(1-\nu)(\varepsilon_I^2+\varepsilon_{II}^2+\varepsilon_{III}^2)+2\nu(\varepsilon_I\varepsilon_{II}+\varepsilon_I\varepsilon_{III}+\varepsilon_{II}\varepsilon_{III})\Big] & \text{in } \Omega_1, \\ \dfrac{E}{2(1-\nu^2)}(\varepsilon_I^2+\varepsilon_{II}^2+2\nu\varepsilon_I\varepsilon_{II}) & \text{in } \Omega_2, \\ \dfrac{1}{2}E\varepsilon_I^2 & \text{in } \Omega_3, \\ 0 & \text{in } \Omega_4. \end{cases} \tag{4}$$

In subdomain Ω_1, where the material behaves like an intact linear elastic isotropic material and no "cracking strain" arise, the conventional contribution $1/2\ (\sigma_I\varepsilon_I + \sigma_{II}\varepsilon_{II} + \sigma_{III}\varepsilon_{III})$ is recovered, where $\varepsilon_I = \varepsilon_I^e$, $\varepsilon_{II} = \varepsilon_{II}^e$ and $\varepsilon_{III} = \varepsilon_{III}^e$ and the generalized 3D Hooke's law holds. In Ω_2, the strain energy $1/2\ (\sigma_I\varepsilon_I + \sigma_{II}\varepsilon_{II})$ is stored in the plane $z_I\ z_{II}$ for $\varepsilon_I = \varepsilon_I^e$ and $\varepsilon_{II} = \varepsilon_{II}^e$. Indeed, the generalized Hooke's law for plane stress holds, while no contribution is related to the orthogonal latent strain along z_{III}. In Ω_3, some strain energy is stored only along the compressive direction z_I, i.e. $1/2\ \sigma_I\varepsilon_I$ with $\varepsilon_I = \varepsilon_I^e$ accounting for the 1D Hooke's law, while the latent strains in the orthogonal plane $z_{II}\ z_{III}$ do not provide any elastic contribution. The "fully cracked" subdomain Ω_4 provides null energy since no stress does work for the latent strain.

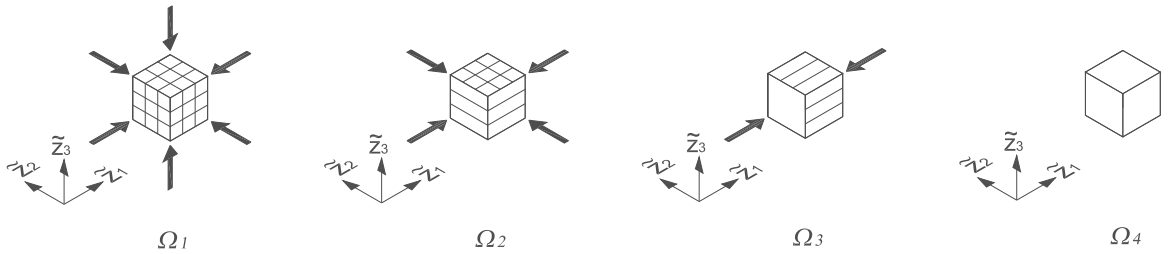

Figure 1: The equivalent orthotropic material with symmetry axes $\widetilde{z}_1$, $\widetilde{z}_2$ and $\widetilde{z}_3$ is oriented along the principal stress directions of the no–tension solid z_I, z_{II} and z_{III} to model its characteristic behavior in the four subdomains Ω_{1-4}. Lines stand for directions where the stiffness of the equivalent composite is not negligible.

2.3. An equivalent composite to mimic the no–tension solid

An equivalent composite can be defined to mimic the behavior of the linear elastic masonry–like solid at any point $\chi \in \Omega$, that means providing for each one of the subdomains Ω_1–Ω_4 the relevant form of the strain energy function $\phi(\underline{\underline{\varepsilon}})$ as defined by Eqn. (3) and Eqn. (4).

An orthotropic material is considered with symmetry axes $\widetilde{z}_i$, $i = 1, 2, 3$. Direction cosines are preferred to Euler's angles to describe the orientation of the material due to their straightforward implementation in the algorithm presented in detail in Sections 3.2 and 3.3. $\mathbf{V} = [\ \widetilde{\mathbf{e}}_1 \mid \widetilde{\mathbf{e}}_2 \mid \widetilde{\mathbf{e}}_3\ ]$ stores the direction cosines of the symmetry axes of the material with respect to the adopted reference system in Ω, i.e. z_i, $= 1, 2, 3$. $\mathbf{V}$ is such that the symmetry axes of the orthotropic material correspond to the principal direction of stress (and strain) of the masonry–like material z_α, $\alpha = I, II, III$, see Figure 1.

$\widetilde{E}_i$, $i = 1, 2, 3$, is the Young's modulus of the composite along the symmetry axis $\widetilde{z}_i$, $\widetilde{G}_{ij}$, $i, j = 1, 2, 3$, is the shear modulus in the symmetry plane $(\widetilde{z}_i, \widetilde{z}_j)$ and $\widetilde{\nu}_{ij}$, $i, j = 1, 2, 3$, is the Poisson's ratio along $\widetilde{z}_j$ under uniaxial tension along $\widetilde{z}_i$. The equalities $\widetilde{\nu}_{12}/\widetilde{E}_1 = \widetilde{\nu}_{21}/\widetilde{E}_2$, $\widetilde{\nu}_{13}/\widetilde{E}_1 = \widetilde{\nu}_{31}/\widetilde{E}_3$ and $\widetilde{\nu}_{23}/\widetilde{E}_2 = \widetilde{\nu}_{32}/\widetilde{E}_{32}$ hold.

Let $\rho_i(\chi)$, $i = 1, 2, 3$, be three bounded functions in Ω, such that $\rho_{min} \leq \rho_1, \rho_2, \rho_3 \leq 1$, respec-

tively, where ρ_{min} is a strictly positive lower bound to avoid any singularity. The elastic properties of the equivalent orthotropic material along its symmetry axes are assumed to be governed by ρ_i, $i = 1, 2, 3$, through an interpolation model that reads:

$$\widetilde{E}_i = \rho_i \, E, \quad \widetilde{\nu}_{ij} = \sqrt{\rho_i/\rho_j} \, \nu, \quad \tilde{G}_{ij} = \sqrt{\rho_i \rho_j} \, G \quad (i, j = 1, 2, 3), \tag{5}$$

where E, ν and $G = E/(2(1+\nu))$ are the Young's modulus, the Poisson's ratio and the shear modulus of the isotropic material, respectively. ρ_i, $i = 1, 2, 3$, can be seen as parameters that govern stiffness transitions along $\widetilde{z}_1$, $\widetilde{z}_2$ and $\widetilde{z}_3$, see e.g. [7]. The above interpolation has especially been conceived to provide vanishing stiffness along any direction onto which a variable achieves its minimum value. Also, it recovers an isotropic material for $\rho_1 = \rho_2 = \rho_3$ and a transversally isotropic material for $\rho_1 = \rho_2$ and $\rho_3 = \rho_{min}$, independently of the value of the repeated governing parameter.

The constitutive law for the orthotropic material may be written in general form as:

$$\sigma_{ij} = C_{ijhk} \left(\rho_1(\chi), \rho_2(\chi), \rho_3(\chi), \mathbf{V}(\chi)\right) \varepsilon_{hk}, \tag{6}$$

where C_{ijhk} is the fourth order elasticity tensor of the equivalent orthotropic material, see e.g. [50]. Using Voigt notation the cartesian components of the stress tensor σ_{ij} are re–gathered in the array $\underline{\sigma} = [\sigma_{11} \, \sigma_{22} \, \sigma_{33} \, \sigma_{31} \, \sigma_{12} \, \sigma_{23}]^T$ and, analogously, $\underline{\varepsilon} = [\varepsilon_{11} \, \varepsilon_{22} \, \varepsilon_{33} \, \gamma_{31} \, \gamma_{12} \, \gamma_{23}]^T$ for the components of the strain tensor ε_{ij}. Recalling that $\widetilde{\underline{\sigma}} = \mathbf{T}(\mathbf{V})\underline{\sigma}$, where $\mathbf{T}(\mathbf{V})$ can be recovered computing $\widetilde{\sigma}_{mn} = V_{im} V_{jn} \sigma_{ij}$ and re–ordering according to Voigt notation, and $\widetilde{\underline{\varepsilon}} = \mathbf{R}\mathbf{T}(\mathbf{V})\mathbf{R}^{-1} = \mathbf{T}^{-T}\underline{\sigma}$, where $\mathbf{R}$ is the Reuter matrix that transforms the tensorial components into Voigt components,

one has:

$$\underline{\sigma} = \mathbf{T}(\mathbf{V})^{-1}\widetilde{\mathbf{C}}(\rho_1,\rho_2,\rho_3)\mathbf{T}(\mathbf{V})^{-T}\underline{\varepsilon} = \mathbf{C}(\rho_1,\rho_2,\rho_3,\mathbf{V})\underline{\varepsilon}, \quad \text{with}$$

$$\widetilde{\mathbf{C}}^{-1} = \begin{bmatrix} \frac{1}{\rho_1 E} & -\frac{1}{\sqrt{\rho_2\rho_1}}\frac{\nu}{E} & -\frac{1}{\sqrt{\rho_3\rho_1}}\frac{\nu}{E} & 0 & 0 & 0 \\ & \frac{1}{\rho_2 E} & -\frac{1}{\sqrt{\rho_3\rho_2}}\frac{\nu}{E} & 0 & 0 & 0 \\ & & \frac{1}{\rho_3 E} & 0 & 0 & 0 \\ & & & \frac{1}{\sqrt{\rho_3\rho_1}G} & 0 & 0 \\ & \text{sym} & & & \frac{1}{\sqrt{\rho_1\rho_2}G} & 0 \\ & & & & & \frac{1}{\sqrt{\rho_2\rho_3}G} \end{bmatrix}, \tag{7}$$

where $\widetilde{\mathbf{C}}^{-1}$ is the compliance matrix of the equivalent orthotropic material written in the system defined by its symmetry axes and $\mathbf{C}^{-1}$ is the resulting compliance matrix in the global reference system.

Specializing $\widetilde{\mathbf{C}}$ in terms of the extremal values of ρ_i, $i = 1, 2, 3$, the behavior found in each one of the four subdomains Ω_1–Ω_4 of Eqn. (3) is shown to be recovered by Eqn. (7), meaning that the strain energy stored in each subdomain is that expected from Eqn. (4). For the sake of simplicity, it is herein assumed that $\widetilde{z}_1 = z_I$, $\widetilde{z}_2 = z_{II}$ and $\widetilde{z}_3 = z_{III}$. For $\rho_1 = \rho_2 = \rho_3 = 1$ the generalized Hooke's law for 3D bodies is recovered (Ω_1); for $\rho_1 = \rho_2 = 1$ and $\rho_3 = \rho_{min}$ a transversally isotropic material undergoing plane stress in z_I z_{II} arises (Ω_2); for $\rho_1 = 1$ and $\rho_2 = \rho_3 = \rho_{min}$ the term $\widetilde{\mathbf{C}}^{-1}_{11}$ turns out to be $1/E$, whereas the other entries provide contributions of negligible stiffness (Ω_3); finally, for $\rho_1 = \rho_2 = \rho_3 = \rho_{min}$ one finds a "void phase" (Ω_4).

Hence, the behavior of the equivalent orthotropic material matches that of the masonry–like solid if the symmetry axes of the composite phase $\widetilde{z}_i$, $i = 1, 2, 3$ are aligned with the principal stress (and strain) directions z_α, $\alpha = I, II, III$, and the relevant parameters ρ_1, ρ_2 and ρ_3 attain

unitary value in case of any principal compressive stress and vanishing value elsewhere. In other words, a penalization of the stiffness of the material is required along the direction of any potential inelastic strain, see Figure 1.

3. Energy–based analysis of no-tension solids

3.1. Problem formulation

As stated in the introduction, the equilibrium of a linear elastic masonry–like solid can be solved searching for the displacement field that minimizes the total potential energy. Let $\Gamma = \Gamma_t \cup \Gamma_u$ denote the boundary of the three–dimensional domain Ω. Γ_t is subjected to tractions $\underline{t}_0$, whereas Γ_u to prescribed displacements $\underline{u}_0$. The body force $\underline{g}_0$ acts in Ω. The minimization problem reads:

$$\min_{\underline{v}\in\underline{v}_{ad}} = \frac{1}{2}\int_\Omega \frac{\partial\phi(\underline{\underline{\varepsilon}}(\underline{v}))}{\partial\varepsilon^e_{ij}(\underline{v})}\varepsilon^e_{ij}(\underline{v})\ d\Omega - \int_{\Gamma_t}\underline{t}_0\cdot\underline{v}\ d\Gamma - \int_\Omega \underline{g}_0\cdot\underline{v}\ d\Omega, \tag{8}$$

where $\underline{v}\in H^1$ is any kinematically admissible vectorfield such that $\underline{v}\mid_{\Gamma_u}=\underline{u}_0$ and $\phi(\underline{\underline{\varepsilon}})$ is specialized in the subdomains $\Omega_{1-4}\in\Omega$ according to Eqns. (3) and (4).

The minimization statement in Eqn. (8) can be reformulated as an energy–based problem involving the equivalent material defined in Section 2.3, see [12] for the 2D rationale. Phases of the composite are distributed in the domain searching for the triplet of the parameters ρ_i, $i=1,2,3$, that minimizes the overall strain energy satisfying the no–tension constraint, i.e.:

$$\begin{cases} \min\limits_{\rho_{min}<\rho_1,\rho_2,\rho_3\le 1} \Phi = \dfrac{1}{2}\displaystyle\int_\Omega \underline{\underline{\varepsilon}}(\underline{u})^T\ \mathbf{C}(\rho_1,\rho_2,\rho_3,\mathbf{V})\ \underline{\underline{\varepsilon}}(\underline{u})\ d\Omega, & \text{(9a)}\\ \displaystyle\int_\Omega \underline{\underline{\varepsilon}}(\underline{u})^T\ \mathbf{C}(\rho_1,\rho_2,\rho_3,\mathbf{V})\ \underline{\underline{\varepsilon}}(\underline{v})\ d\Omega = \int_{\Gamma_t}\underline{t}_0\cdot\underline{v}\ d\Gamma + \int_\Omega \underline{g}_0\cdot\underline{v}\ d\Omega, & \text{(9b)}\\ \mathbf{V}|\ \tilde{z}_1 = z_I, \tilde{z}_2 = z_{II}, \tilde{z}_3 = z_{III}, & \text{(9c)}\\ \rho_1,\rho_2,\rho_3 \mid \sigma_I,\sigma_{II}\,\sigma_{III}\le 0. & \text{(9d)} \end{cases}$$

In the above formulation Eqn. (9b) holds $\forall \underline{v} \in H^1$ such that $\underline{v} \mid_{\Gamma_u} = \underline{u}_0$ to state the stationarity condition of the primal variational principle, whereas Eqns. (9c-9d) enforce that the overall strain energy of the equivalent composite computed through Eqn. (9a) corresponds to that of the linear elastic no–tension material.

According to Eqn. (9b) a displacement–based discretization made of N finite elements is adopted in the simulations. The element–wise minimization unknowns x_{e1}, x_{e2}, x_{e3} are the parameters governing the stiffness of the equivalent material along its symmetry axes. In the e–th finite element, these axes are defined by the matrix of the direction cosines $\mathbf{V}_e$. The arising discrete formulation reads:

$$
\begin{cases}
\min\limits_{x_{min} \le x_{e1}, x_{e2}, x_{e3} \le 1} \Phi = \dfrac{1}{2} \displaystyle\sum_{e=1}^{N} \mathbf{U}_e^T \mathbf{K}_e(x_{e1}, x_{e2}, x_{e3}, \mathbf{V}_e) \mathbf{U}_e, & \text{(10a)} \\
\displaystyle\sum_{e=1}^{N} \mathbf{K}_e(x_{e1}, x_{e2}, x_{e3}, \mathbf{V}_e) \mathbf{U}_e = \mathbf{F}, & \text{(10b)} \\
\mathbf{V}_e \mid \tilde{z}_1 = z_I, \tilde{z}_2 = z_{II}, \tilde{z}_3 = z_{III}, \quad e = 1 \dots N, & \text{(10c)} \\
x_{e1}, x_{e2}, x_{e3} \mid \sigma_I, \sigma_{II}\, \sigma_{III} \le 0, \quad e = 1 \dots N. & \text{(10d)}
\end{cases}
$$

The objective function is computed over the N elements of the mesh, $\mathbf{K}_e$ and $\mathbf{U}_e$ being the element stiffness matrix and the vector of the nodal displacements of the e–th element, respectively. $\mathbf{F}$ denotes the vector gathering the nodal load contributions. Eqn. (10b) enforces elastic equilibrium in Ω for any set of the discrete minimization unknowns, whereas Eqn. (10c) prescribes that the symmetry axes of the equivalent orthotropic material are aligned to the principal stress directions of the no–tension solid. Eqn. (10d) requires the discrete minimization unknowns to define a compression–only stress state all over the domain. The lower bound $x_{min} = 10^{-5}$ is assumed in the simulations.

The above problem can be handled through mathematical programming techniques, such as

sequential convex programming, in order to solve the equilibrium for any compatible set of dead and live loads without accounting for the previous load history. By repeating the minimization call for different values of the live loads, the collapse load of the structural element can also be estimated as the value beyond which convergence is lost, see in particular [13].

3.2. Solving algorithm

Algorithm 1

procedure NoTen3D
  Set $j = 0, \quad \Phi^j = \infty, \quad \Delta\Phi = 1$
  Initialize $x_{ie}^j = 0.5$ $i = 1, 2, 3$ and $\mathbf{V}_e^j = \mathbf{I}$, $\forall e$
  while $\Delta\Phi > \Delta\Phi_{tol}$ **do**
    $j = j + 1$
    Assign $\mathbf{C}_e^{-1}(x_{e1}^{j-1}, x_{e2}^{j-1}, x_{e3}^{j-1}, \mathbf{V}_e^{j-1})$, $\forall e$
    Solve $\sum_N \mathbf{K}_e(x_{e1}^{j-1}, x_{e2}^{j-1}, x_{e3}^{j-1}, \mathbf{V}_e^{j-1})\mathbf{U}_e = \mathbf{F}$
    Compute Φ^j, $\sigma_{eg\alpha}$ $\alpha = I, II, III$ at Gauss points, $\mathbf{V}_e^j$ at the center, $\forall e$
    Evaluate $\Delta\Phi = |\sum_N \Phi_e^j - \sum_N \Phi_e^{j-1}|/|\sum_N \Phi_e^{j-1}|$
    Set $\widehat{w}_{\alpha\beta}$, at each Gauss point, $\forall e$, such that:

$$\begin{cases} \widehat{w}_{eg\alpha\beta} = w_{eg}, & \text{if } \sigma_{eg\alpha} \leq 0 \wedge \sigma_{eg\beta} \leq 0, \\ \widehat{w}_{eg\alpha\beta} = -k w_{eg}, & \text{otherwise.} \end{cases}$$

    Compute $\dfrac{\widehat{\partial\Phi}}{\partial x_{ei}} = -\dfrac{1}{2}\displaystyle\sum_{n_g} \widehat{w}_{eg\alpha\beta}\ \sigma_{eg\alpha}\frac{\partial\widetilde{C}_{\alpha\beta}^{-1}}{\partial x_{ei}}\sigma_{eg\beta}\ \det\mathbf{J}_e \quad \alpha, \beta = I, II, III$, $\forall e$
    Update x_{ei}, $i = 1, 2, 3$, $\forall e$ as:

$$\begin{cases} x_{ei}^j = \max[x_{ei}^{j-1} - \xi, x_{min}], & \text{if } x_{ei}^{j-1} - \gamma\dfrac{\widehat{\partial\Phi}}{\partial x_{ei}} < \max[x_{ei}^{j-1} - \xi, x_{min}], \\ x_{ei}^j = \min[x_{ei}^{j-1} + \xi, x_{max}], & \text{if } x_{ei}^{j-1} - \gamma\dfrac{\widehat{\partial\Phi}}{\partial x_{ei}} > \min[x_{ei}^{j-1} + \xi, x_{min}], \\ x_{ei}^j = x_{ei}^{j-1} - \gamma\dfrac{\widehat{\partial\Phi}}{\partial x_{ei}}, & \text{otherwise.} \end{cases}$$

  end while
  Assign $\mathbf{C}_e^{-1}(x_{e1}^j, x_{e2}^j, x_{e3}^j, \mathbf{V}_e^j)$, $\forall e$
  Solve $\sum_N \mathbf{K}_e(x_{e1}^j, x_{e2}^j, x_{e3}^j, \mathbf{V}_e^j)\mathbf{U}_e = \mathbf{F}$
  Compute and plot $\sigma_{eg\alpha}$, $\alpha = I, II, III$ at Gauss points, $\mathbf{V}_e$ at the center, $\mathbf{U}_e$ at nodes, $\forall e$
end procedure

The minimization statement in Eqn. (10) can be solved by adopting optimality criteria instead of mathematical programming, see e.g. [27]. At each iteration of the update scheme, the derivatives of the objective function with respect to the minimization unknowns are required. By means of the adjoint method, the sensitivities of the strain energy may simply be retrieved from the current finite element solution as:

$$\frac{\partial \Phi}{\partial x_{ei}} = -\frac{1}{2}\mathbf{U}_e^T \frac{\partial \mathbf{K}_e}{\partial x_{ei}} \mathbf{U}_e. \tag{11}$$

Due to Eqn. (1c) the strain energy is equivalent to the complementary energy, meaning that the above sensitivity may alternatively be written in terms of stresses as:

$$\frac{\partial \Phi}{\partial x_{ei}} = -\frac{1}{2} \int_{V_e} \underline{\sigma}_e^T \frac{\partial \mathbf{C}_e^{-1}}{\partial x_{ei}} \underline{\sigma}_e \; dV, \tag{12}$$

where $\underline{\sigma}_e$ collects the cartesian components of the stress tensor σ_{ij} in the e–th finite element of volume V_e according to Voigt notation. For each element, the compliance matrix of the equivalent orthotropic material $\mathbf{C}_e^{-1}$ depends on x_{e1}, x_{e2}, x_{e3} and $\mathbf{V}_e$, see Eqn. (6).

Eqn. (12) can be evaluated from the current finite element solution by computing the principal stresses $\sigma_{eg\alpha}$ (with $\alpha = I, II, III$) in the g–th Gauss point of the e–th element and exploiting numerical integration as follows:

$$\frac{\partial \Phi}{\partial x_{ei}} = -\frac{1}{2} \sum_{g=1}^{n_g} w_{eg} \; \sigma_{eg\alpha} \frac{\partial \widetilde{C}_{e\alpha\beta}^{-1}}{\partial x_{ei}} \sigma_{eg\beta} \; \mathrm{det}\mathbf{J}_e, \quad \text{with } \alpha, \beta = I, II, III. \tag{13}$$

In the above equation, w_{eg} is the weight related to the g–th among the n_g Gauss points within the element, $\mathbf{J}_e$ is the Jacobian of the element and the terms $\widetilde{C}_{e\alpha\beta}^{-1}$ are suitable entries of the element compliance matrix $\widetilde{\mathbf{C}}_e^{-1}$ written in terms of the symmetry axes of the equivalent material. These entries depends on x_{e1}, x_{e2}, x_{e3} only, according to Eqn. (7).

To enforce the compression–only stress regime, modified sensitivities $\partial\widehat{\Phi}/\partial x_{ei}$ can conveniently be adopted to govern a steepest descent–like optimization algorithm and solve Eqn. (10) without implementing Eqn. (10d) as a set of local constraints. The resulting algorithm is equivalent to the optimality criteria method used in many problems of structural optimization, see in particular [7] and [2].

The modified sensitivities are computed by substituting in Eqn. (13) the term w_{eg} with the following $\widehat{w}_{eg\alpha\beta}$:

$$\begin{cases} \widehat{w}_{eg\alpha\beta} = w_{eg}, & \text{if } \ \sigma_{eg\alpha} \leq 0 \wedge \sigma_{eg\beta} \leq 0, \\ \widehat{w}_{eg\alpha\beta} = -k w_{eg}, & \text{otherwise}, \end{cases} \tag{14}$$

with $k \in (0, 1]$ and $k = 0.5$ in the numerical simulations presented in Section 4.

The proposed numerical scheme is implemented in a procedure called NoTen3D, which is detailed in Algorithm 1.

At iteration $j = 0$, the minimization variables $x_{e1} = x_{e2} = x_{e3}$ are given the initial guess 0.5 to define an isotropic material no matter the assignment of $\mathbf{V}_e$, see Eqn. (7). The array which stores the strain energy values Φ during each step of the algorithm is initialized, as well as the scalar quantity $\Delta\Phi$ that records the relative change in energy between two subsequent iterations.

A main set of instructions is repeated within the loop from lines 4 to 13 to update the element–wise minimization unknowns and the orientations matrices of the equivalent material. At each iteration j, the compliance matrices $\mathbf{C}_e^{-1}$ are evaluated depending on the current set of x_{e1}, x_{e2}, x_{e3} and $\mathbf{V}_e$ through Eqns. (6–7). The global stiffness matrix is assembled and inverted to compute the unknown nodal displacements in each element vector $\mathbf{U}_e$, see lines 6-7.

The overall strain energy is calculated to evaluate its variation with respect to the previous iteration, which is stored in $\Delta\Phi$. The principal stress directions z_I, z_{II} and z_{III} are computed at the center of the element to update $\mathbf{V}_e$, whereas the principal stresses are evaluated at each Gauss

point to compute the modified sensitivities $\widehat{\partial\Phi}/\partial x_{ei}$ according to Eqns. (13) and (14), see lines 10-11. This is done by solving a set of eigenvalue problems after evaluating the component of the stress tensor at the points above mentioned. The steepest descent–like update scheme is reported in line 12: the move limit ξ defines the maximum variation that a minimization unknown can attain within a single step, whereas γ scales the gradient information. In the numerical simulations it is assumed that $\xi = 0.2$ and $\gamma = 0.5$. Both user–defined parameters can be tuned to fix convergence issues as well as speed up the procedure, if needed. In general, lowering ξ and γ allows a smoother history of the objective function to be obtained, whereas more iterations of the algorithm are performed.

In case the stopping criterion $\Delta\Phi \leq \Delta\Phi_{tol}$ is met, the compliance matrices $\mathbf{C}_e^{-1}$ are evaluated depending on the last set of minimization variables x_{e1}, x_{e2}, x_{e3} and direction cosines $\mathbf{V}_e$, which provide the expected equivalence of the fictitious orthotropic material with respect to the linear elastic masonry–like medium. Hence, the stiffness matrix $\mathbf{K}$ is assembled and inverted to evaluate the displacement and the stress field that solve the no–tension elasticity problem (lines 14-16). $\Delta\Phi_{tol} = 10^{-3}$ is adopted in the numerical simulations.

It is finally remarked that the constrained minimization statement in Eqn. (10) could be alternatively solved resorting to derivative–free algorithm, see e.g. [39, 18].

3.3. Implementation through the API of a finite element package

The proposed algorithm can straightforwardly be implemented to exploit the Application Programming Interface (API) of any general purpose software that performs the Finite Element Analysis (FEA) for linear elastic orthotropic media. Using communication protocols, few input and output data are exchanged between an external program and the FEA package to iteratively run the analyses of the equivalent composite with space–varying properties.

The steps needed to perform the process are sketched in the flowchart shown in Figure 2.

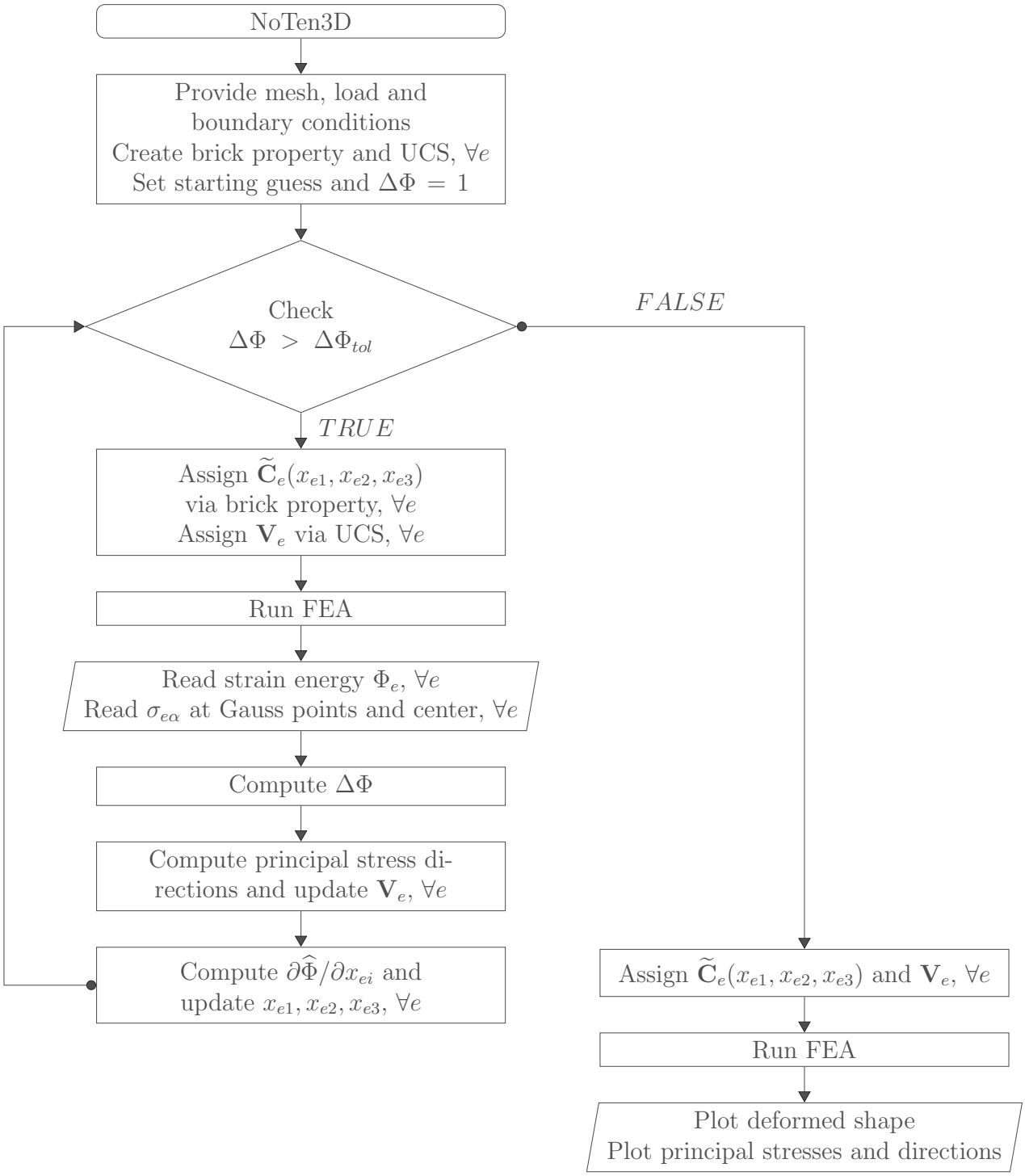

Figure 2: Flowchart of NoTen3D as implemented using the API of a finite element package.

At first, the model is built (or imported) in the FEA software environment, providing a three–dimensional mesh made of brick elements from the available library, and prescribing loads and boundary conditions. The case of a general purpose FEA software that does not allow the API to access the element stiffness matrix is herein considered. To overcome this issue, a new brick property is assigned to each element in the mesh, along with a relevant User Coordinate System (UCS). The former permits control of the elastic constants of an orthotropic material model, whereas the latter provides information on the alignment of the symmetry axes of the composite with respect to the global reference system. The initialization of the algorithm is performed as described in the previous section.

At each iteration, the current set of parameters x_{e1}, x_{e2}, x_{e3} is needed to endow the brick properties with the relevant compliance matrices $\widetilde{\mathbf{C}}_e^{-1}$, which are written in terms of the material reference systems according to Eqn. (7). The current set of direction cosines $\mathbf{V}_e$ enters the assignment of the relevant UCSs to align the composite element by element. Afterwards, the built–in solver is used to perform a finite element analysis and post–process the solution to provide an approximation of the stress field and compute the variation in terms of the overall strain energy with respect to the previous iteration. The principal stress directions read at the center of the elements directly provide a new set of matrices $\mathbf{V}_e$, whereas the principal stresses read at the Gauss points of each element allow for the computation of the modified sensitivities required by the scheme used to update the minimization variables.

At convergence, the graphical user interface (GUI) of the software package can be fully exploited to provide stress and displacement maps by post–processing the solution achieved.

4. Numerical simulations

Extended simulations are reported to assess the implemented algorithm, focusing both on numerical features and applications. Section 4.1 addresses different sets of control points for

the constitutive properties of the equivalent material, investigating the effect of mesh refinement. Section 4.2 focuses on the collapse of a windowed masonry panel subjected to vertical and out–of–plane loads, providing a comparison with results from limit load analysis. Sections 4.3 and 4.4 show load paths computed by the proposed method in cracked masonry vaults for different load scenarios.

Conventional bilateral restraints can be used in conjunction with the linear elastic no–tension material model. Supports and symmetry conditions can be dealt with by prescribing one or more null components of the nodal displacements, i.e. by removing the relevant degrees of freedom and the related sub-vectors and sub–matrices in Eqn. (10b). Only negative semi–definite stresses are allowed within the no-tension solid, meaning that tensile reactions can not occur. In case there is no compressive stress in the vicinity of the boundary, inelastic strains arise to recover kinematics. This provides the expected unilateral behaviour of the restraints.

4.1. Example 1. A square column under eccentric loading

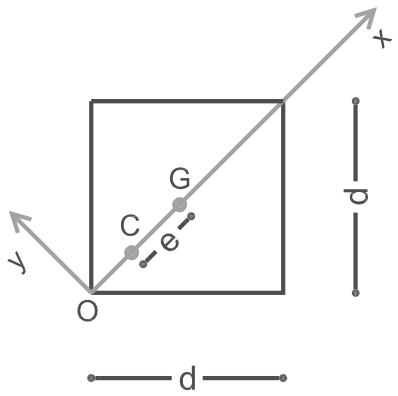

Figure 3: Example 1. Section of a column subject to an eccentric force.

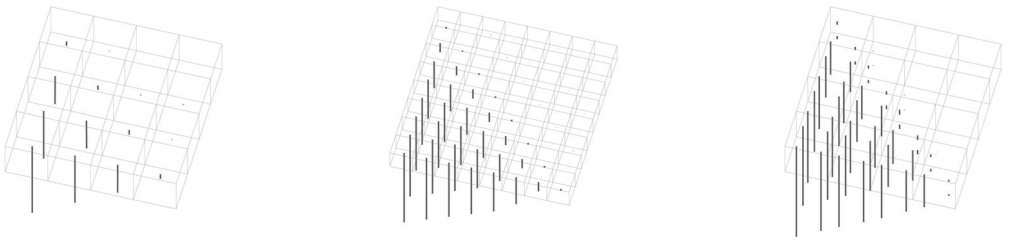

(a) (b) (c)

Figure 4: Example 1. Principal stress directions for different meshes and control points of the constitutive properties of the equivalent material: element–based approach with 4x4x16 elements (a); element–based approach with 8x8x32 elements (b); 4x4x16 elements and implementation based on Gauss points (c).

A preliminary investigation is performed on a square column of height $H = 1.2$ m, with side $d = 0.3$ m. Its section is shown in Figure 3. The column is made of two different materials: from the base to the height of 0.95 m, the column is made of a masonry–like material with $E_m = 1,000$ MPa and $\nu_m = 0.25$, whereas the upper part is made of a material symmetric in tension and compression, with $E_c = 100E_m$ and $\nu_c = \nu_m$. A vertical load $P = 10$ kN is applied at the top in the center of pressure C, which is eccentric with respect to the center of gravity G because of $e = \sqrt{2}d/4$. The objective of the top "curb" is to spread the vertical load and constrain the underlying horizontal sections of the masonry–like column to remain plain. Vertical displacements are restrained at the base of the column.

Combined compressive and bending stresses σ_{zz} arise in the solid, being z the vertical axis. Due to the symmetry properties of the section, the compression-only stress field is expected to be linear in x–direction and constant along the orthogonal y–direction. The translational equilibrium along the z–axis and the rotational equilibrium around the y–axis provide $x_n = 2e = \sqrt{2}d/2 = 0.212$ m and $\overline{\sigma}_z^- = 3N/(4e^2) = 6N/d = -0.667$ MPa, where x_n defines the location of the neutral axis and $\overline{\sigma}_z^-$ the minimum stress. Hence, half of the section undergoes compressive stresses that are linear in the x–direction and vanish along the orthogonal diagonal.

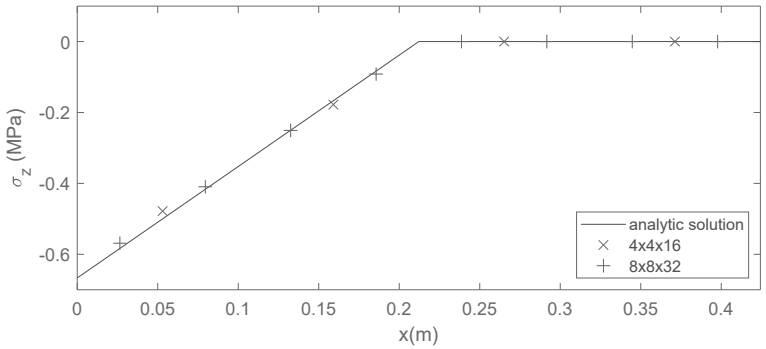

Figure 5: Example 1. Normal stress σ_{zz} along the x–axis: analytical solutions vs. values computed in the center of the elements for the element–based approach with meshes 4x4x16 and 8x8x32.

Figure 4 provides a comparison in terms of computed principal stress directions in a typical section of the column. Vectors are drawn at the points where the stress field is evaluated to control the orientation of the equivalent orthotropic material (in general, the center of the element). They lie along the principal stress directions and their length is proportional to the value of the stress. The map is scaled by the maximum value computed in the domain under the load condition considered. The same considerations apply to all similar maps reported in the following. Different set of points to control the constitutive properties of the equivalent material are considered in this figure, as well as different meshes. Sub–figures (a) and (b) refer to the algorithm that computes $\mathbf{V}_e$ at the center of each element to govern the stiffness of the whole element as described in Sections 3.2 and 3.3, whereas sub–figure (c) shows the output of a more complex implementation that controls the constitutive properties of the equivalent material in each Gauss point. In the latter case $N \cdot n_g$ minimization unknowns are used and the formula in Eqn. (13) is evaluated using the stress of the relevant Gauss point only. This approach can not be implemented into a general purpose FEA software that does not allow the API to access the element stiffness matrix or, more generally, to control the constitutive law at each Gauss point.

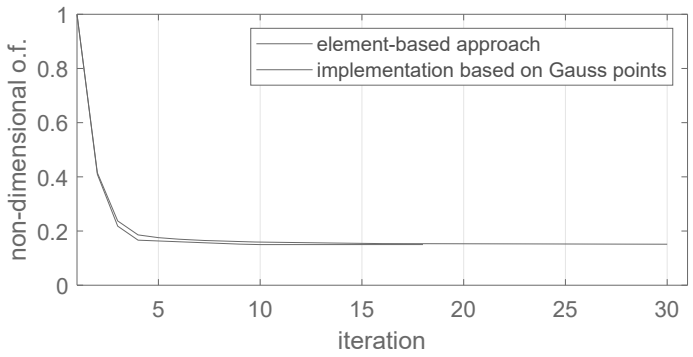

Figure 6: Example 1. History plot of the non–dimensional objective function with 4x4x16 elements: element–based approach vs. implementation based on Gauss points.

Figure 5 shows that normal stresses computed using the former approach on a 4x4x16 and a 8x8x32 elements mesh are in good agreement with the analytical solution. For both meshes, the element–based approach captures effectively the extension of the cracked region and provides a good approximation of the compressive stresses.

Figure 6 provides history plots of the objective function, i.e. the overall strain energy scaled by its value at $j = 1$ for $x_{e1} = x_{e2} = x_{e3} = 0.5$, comparing the element–based approach with the one relying on Gauss points for a mesh with 4x4x16 elements. The algorithm stops when a prescribed tolerance on the maximum relative variation in terms of energy $\Delta\Phi$ is achieved between two subsequent iterations, see Section 3.2. Usually, 10–20 steps are enough to reach convergence. Two smooth curves result from this comparison. However, the element–based method converges faster than the one based on the approximation of the constitutive properties of the material at Gauss points.

The element–based algorithm can be easily implemented in almost every general purpose finite element software that has a linear elastic solver for orthotropic materials and a basic API. Also, it is effective in approximating the expected stress field with smooth and fast convergence. The

simulations presented next will resort to this approach only.

4.2. Example 2. A masonry–like panel subject to out–of–plane live loads

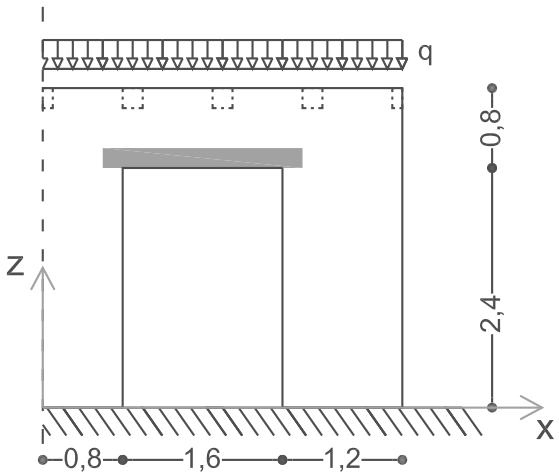

Figure 7: Example 2. Geometry of half of a panel subjected to vertical dead loads and out–of–plane live loads. Dimensions in m.

A façade made of linear elastic masonry–like material is considered: half of the in–plane geometry is shown in Figure 7 considering a plan length $L = 3.6$ m (the panel has a symmetry axis at $x = 0$). The façade has an out–of–plane thickness $s = 0.4$ m. Properties of the material are as follows: $E_m = 1,000$ MPa, $\nu_m = 0.25$, $\gamma_m = 20$ kN/m^3. A lintel made of material with symmetric behavior in tension and compression is modeled over the opening assuming $E_l = 10E_m$, $\nu_l = \nu_m$ and $\gamma_l = \gamma_m$. At the top of the panel the distributed dead load $q = 5$ kN/m acts along the centerline of the wall.

A preliminary analysis is performed accounting for dead loads, i.e. q and self–weight. A map of the principal stress direction is represented in Figure 8 that also provides information on the relative stress magnitude. Principal stresses in compression are marked in blue, whereas principal

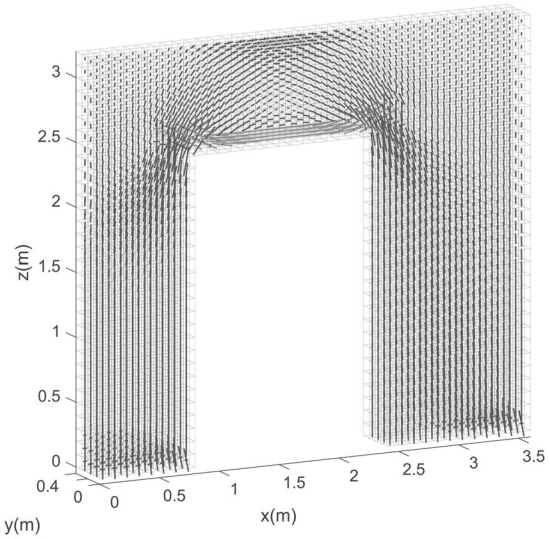

Figure 8: Example 2. Principal stresses in the panel under dead loads. Blue stands for compression, red for tension.

stresses in tension in red. The adopted material model is able to capture an arch–like load path and some stress concentrations arising around the corner of the lintel that absorbs most of the lateral thrust of the arch.

To assess the safety of the façade in case of an earthquake, many technical codes suggest to investigate the activation of first–mode mechanisms induced by out–of–plane loads, see in particular [21]. Assuming a very poor connection between the façade and both the transversal walls and the storey/roof at the top of the panel, an overturning of the wall about its base is expected. The kinematic approach of limit analysis for mechanisms consisting of rotating rigid blocks is considered. Hence, the collapse load multiplier λ_c of the single–degree–of–freedom mechanism reported in Figure 9 is found when the virtual power of the represented forces vanishes. One has:

$$\lambda_c = \frac{(W + qL) \cdot s/2}{W \cdot z_g + qL \cdot H}. \tag{15}$$

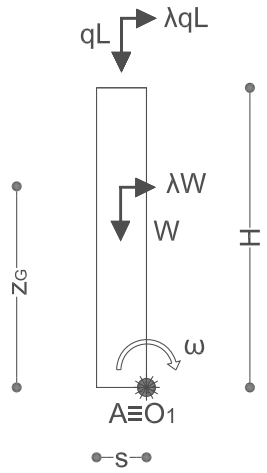

Figure 9: Example 2. Kinematics for the computation of the collapse load multiplier of the panel using limit load analysis.

Considering the geometrical parameters shown in Figure 7 and masses and loads previously defined, $\lambda_c = 0.09$. This means that the façade is likely to overturn under the occurrence of horizontal loads whose magnitude is less than 10% of that of the vertical loads. As already mentioned, limit load analysis is based on the Heyman's model of material, i.e. the rigid no–tension material.

Alternatively, the linear elastic masonry–like material model may be implemented to predict collapse. Solving the equilibrium for λ multiples of 0.01, the last converged value is $\lambda_c = 0.08$, in good agreement with the above analytical result. Figure 10 shows a map of the principal stresses in the panel at incipient collapse along with the (magnified) deformed geometry. The panel is going to overturn almost rigidly about its foot, whereas a "plastic hinge" is going to arise due to the localization of compressive stresses along the edge of the base sections. Figure 10(a) shows also the force path in the lintel, where non–homogeneous tensile stresses allow the sustained regions to transfer both vertical and horizontal loads to the piers. Technical codes may require the evaluation

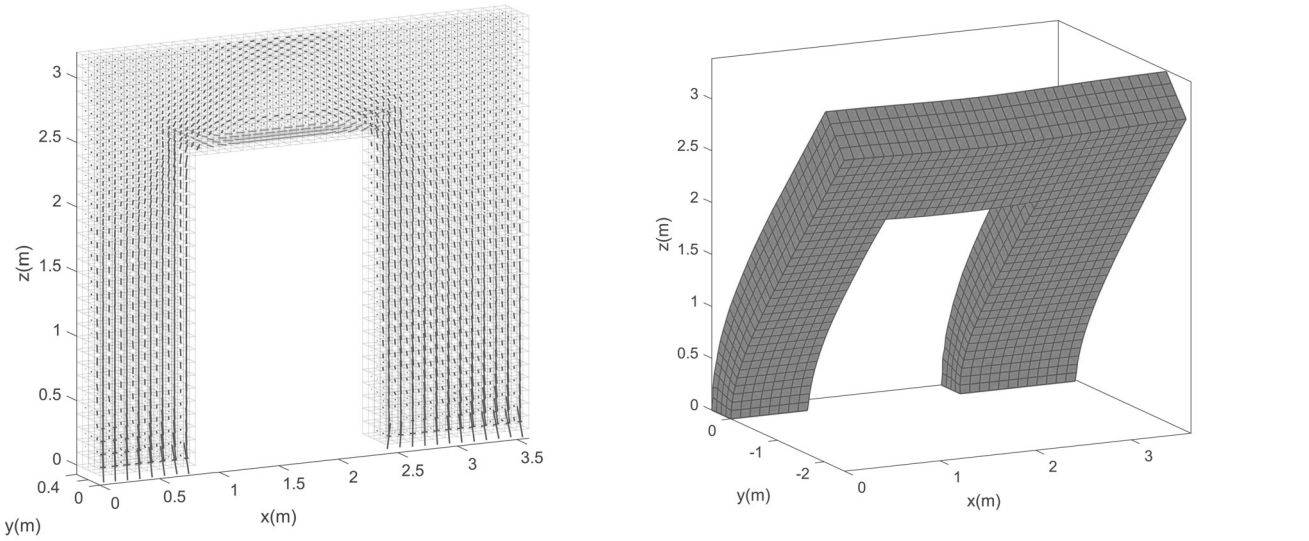

(a) (b)

Figure 10: Example 2. Equilibrium of the panel for $\lambda_c = 0.08$: principal stresses (a) and magnified deformed geometry (b).

of the relevant "spectral seismic acceleration" referring to an equivalent single–degree–of–freedom oscillator. This information is recovered by scaling λ_c by a confidence factor and a "participating mass fraction" that can be straightforwardly evaluated from the horizontal displacements, see the deformed shape in Figure 10(b).

To increase the strength of the façade in case of an earthquake, the connection of the panel with the above storey/roof can conveniently be improved. The effect of a set of ties (end–plate anchors 0.2 m $\times$ 0.2 m, spacing 0.9 m) is modelled enforcing constrained transversal displacements (along y) where anchors act at the top of the wall, see dotted lines in Figure 7. The effect of a longitudinal chain is also modelled, constraining displacements along x in the upper part of the corner at $x = 3.6$ m.

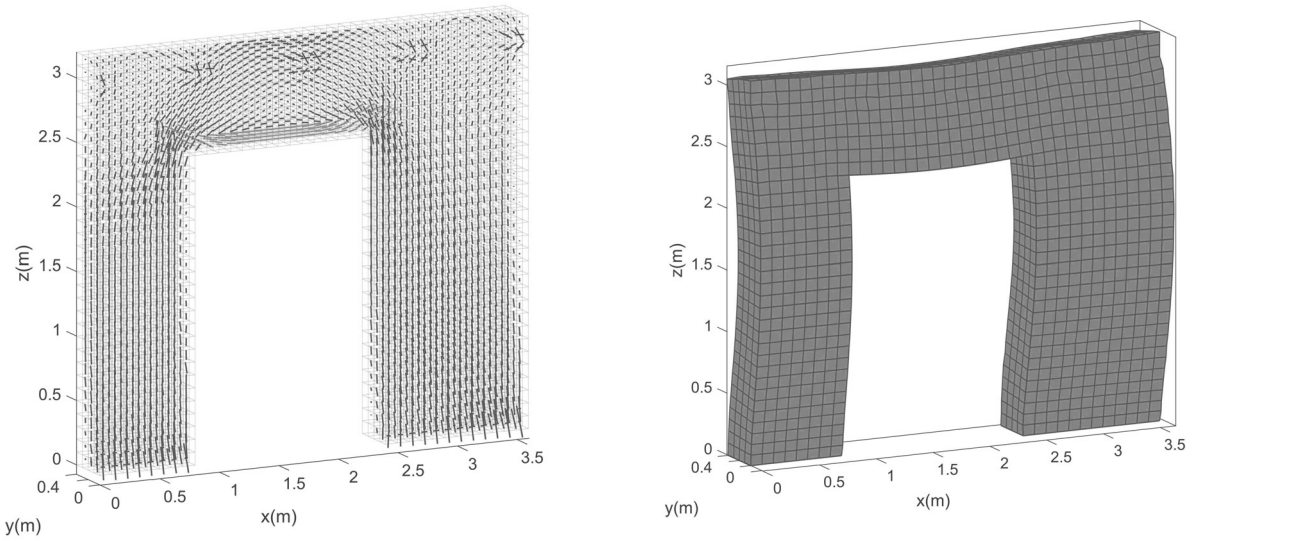

Figure 11: Example 2. Equilibrium of the panel reinforced with ties for $\lambda = 0.45$: principal stresses (a) and magnified deformed geometry (b).

Figure 11 shows a map of the principal stresses in the panel along with a (magnified) deformed geometry for $\lambda = 0.45$. Most of the bulk of the panel is stressed, meaning that the façade is safe for such a remarkable level of horizontal forces, see in particular Figure 12 that refers to a vertical section of the piers. The ties restrain the top wall displacements, while counteracting the effect of the distributed horizonal load λq. Reference is made to Figure 13 that shows arch–like load paths which arise in a horizontal section of the panel located at the height of the transversal ties. This also clarifies the need for a longitudinal constraint/reinforcement to enforce the equilibrium of the corner region. Of course, the effectiveness of the intervention mainly depends on the compressive strength of the masonry–like material (see in particular stress peaks at the anchor regions and at the base of the wall) and on the maximum tensile force that ties can sustain. The proposed procedure

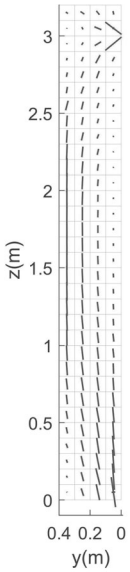

Figure 12: Example 2. Equilibrium of the panel reinforced with ties for $\lambda = 0.45$: principal stress at $x = 2.75$ m.

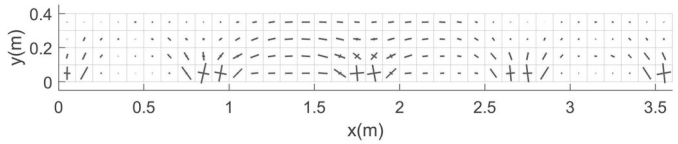

(a)

Figure 13: Example 2. Equilibrium of the panel reinforced with ties for $\lambda = 0.45$: principal stresses at $z = 3.05$ m.

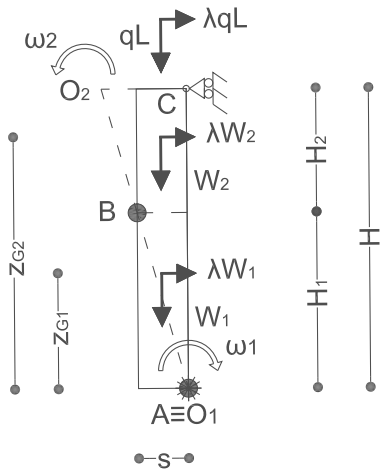

Figure 14: Example 2. Kinematics for the computation of the collapse load multiplier of the panel reinforced with ties using limit load analysis.

can be used to estimate the maximum stress in the no–tension material and the maximum reactions in the constrained regions, i.e. 0.35 MPa and 5.80kN respectively.

Assuming the Heyman's masonry model and excluding failure of ties, one can investigate the load multiplier that activates the two-block collapse mechanism depicted in Figure 14. Block 1 undergoes clockwise instantaneous rotation with velocity ω_1, whereas block 2 rotates anticlockwise with instantaneous velocity ω_2, being $\omega_2 = H_1/H_2\omega_1$. Equilibrium of the partially constrained structure requires vanishing of the virtual power of the depicted forces, that means:

$$\lambda_c = \frac{(qL + W_2)(s/2 + s \cdot H_2/H_1) + W_1 \cdot s/2 \cdot H_2/H_1}{W_2 \cdot (H - z_{g2}) + W_1 \cdot z_{g1} \cdot H_2/H_1}. \tag{16}$$

The value of λ_c depends on the position of the "plastic hinge" in B (i.e. the ratio H_1/H_2), which is not known *a–priori* and can be found by applying the upper bound theorem of limit analysis. The

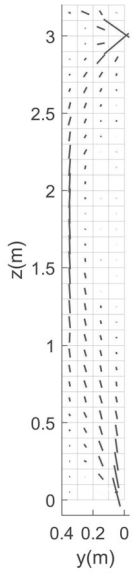

Figure 15: Example 2. Equilibrium of the panel reinforced with ties for $\lambda_c = 0.81$: principal stress at $x = 2.75$ m.

above expression takes a minimum in the interval $0 \leq z \leq 2.4$ m, for $z = 2.15$ m with $\lambda_c = 0.85$. Investigations on the collapse of the panel reinforced with ties have been performed through the proposed energy–based approach implementing the linear elastic masonry–like material model. Figure 15 shows the principal stresses arising in a vertical section of the panel for $\lambda_c = 0.81$, value above which no-tension–free equilibrium solution is found by the implemented algorithm. No assumption is required to detect the position of the central hinge, herein approximately at $z = 2.00$ m.

Finally, Figure 16 shows history plots of the non–dimensional objective function for the solution of the equilibrium of the considered panel under different loads and boundary conditions. The simulation for dead loads ($\lambda = 0$) requires only ten iterations. When looking at the horizontal actions, the handling of loads that precede an incipient collapse requires a few additional steps. In

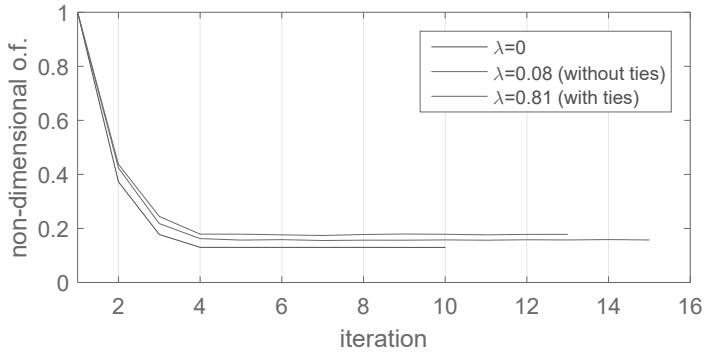

Figure 16: Example 2. History plot of the non–dimensional objective function for the solution of the equilibrium of the panel under different loads and boundary conditions.

the case of both the unreinforced wall and the retrofitted one, curves remain smooth and exhibit a convergence rate that is approximately comparable.

4.3. Example 3. Equilibrium of a cracked hemispherical dome

The hemispherical dome in Figure 17 is considered. The dome has an external radius $R_e = 5$ m, an internal radius $R_i = 4$ m and a thickness $t = 1$ m, i.e. an average radius $R = 4.5$ m and a thickness ratio t/R=0.2. The masonry dome is subject to self–weight, where $\gamma_m = 20$ kN/m^3. Displacements are fully restrained for all the nodes at $z = 0$. A quarter of the dome has been discretized using a mesh of 2592 six–node and eight–node finite elements. Each element spans $\Delta\phi = 3.75°$ in terms of polar angle (colatitude) and $\Delta\theta = 5°$ in terms of azimuthal angle. To enforce a compatible load, the i–th node of the extrados is loaded by the weight of the "voussoir" highlighted in Figure 17, i.e.:

$$w_i = \gamma \frac{\Delta\theta}{3}(R_e^3 - R_i^3)(cos\phi - cos(\phi + \Delta\phi)), \tag{17}$$

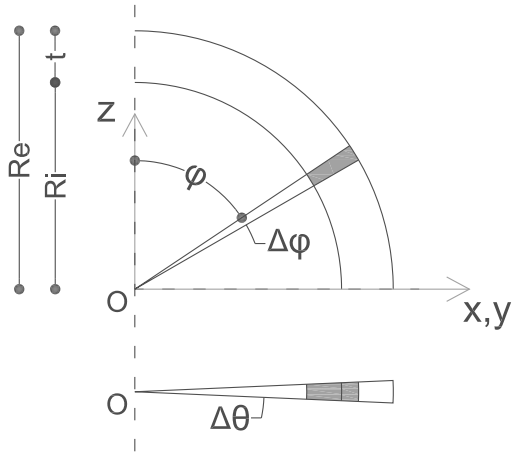

Figure 17: Example 3. Geometry of a hemispherical dome and a typical "voussoir" in section and plan.

see e.g. [51]. Thin uncracked domes under self–weight are generally handled resorting to the membrane theory equations that highlight the meridional and hoop forces that develop. While the former are compressive, the latter take a maximum in compression at the crown and a maximum in tension at the base, with sign reversal at $\phi = 51.8°$, see e.g. [9]. When tensile stresses in the hoop rings at the springing overcome the masonry's weak tensile strength, the membrane equilibrium is lost. Meridian cracks are expected to spread along the lower band of the dome for a latitude that is much higher than the one identifying the tensile–stressed region found in the uncracked dome, see [28].

Cracked domes have been extensively dealt with by resorting to the rigid no–tension material model, see in particular [29] and [30]. In this regard, reference is made to [49] that provides a comprehensive review of the methods derived from the lower and upper bound theorems of limit analysis, i.e. inspired by the concepts of equilibrium and occurrence of failure respectively. Among the others, the work in [16] extends the problem of the catenary to the three–dimensional framework to investigate pressure surfaces of minimum thrust with zero hoop stresses. The modified thrust

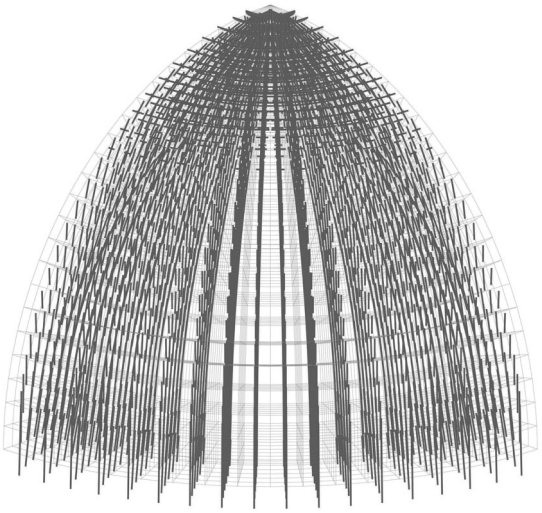

Figure 18: Example 3. Equilibrium of a cracked emispherical dome under self weight: principal compressive stresses in the dome.

line method in [31, 51] allows the designer to search for different combinations of meridional and hoop forces among the infinite range of compressive solutions that the hyperstatic dome can exhibit. The assessment is performed in the spirit of the lower bound theory, meaning that the detection of any feasible equilibrium solution results in the conclusion that the structure is safe. Reference is also made to [23] where cracked masonry domes are considered as no–tension membranes (thrust surfaces) carrying a discrete network of compressive singular stresses.

The equilibrium of the cracked dome is handled through the numerical procedure presented in Section 3. The Young's modulus of the linear elastic–masonry like material is assumed as $E_m = 1,000$ MPa, whereas $\nu_m = 0$. Figure 18 shows the principal stresses of the compression–only solution found at convergence for the quarter of the dome under investigation, whereas Figure 19 refers to the typical lune $\Delta\theta = 5°$. Meridional forces flow from the crown to the base approaching the extrados at the crown and at the springer, and the intrados close to the haunches. Hoop

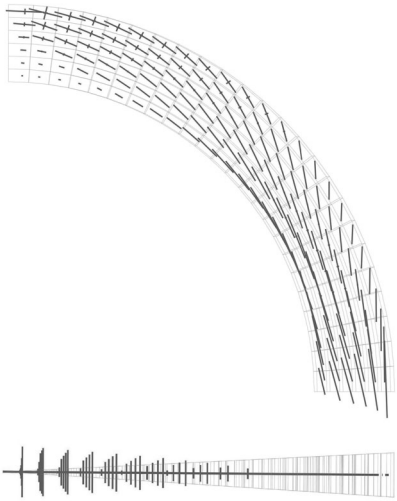

Figure 19: Example 3. Equilibrium of a cracked emispherical dome under self weight: principal compressive stresses in a typical lune (side view and plan).

stresses decreases from their maximum value at the crown to zero, approximately at a colatitude of 40°. They are not constant in the thickness, decreasing from the extrados to the intrados. Looking at the base, integrating the vertical and horizontal reactions, one obtains the unit per length forces $V = 93.1$ kN/m and $H = 15.5$ kN/m, respectively.

A wide set of cracked domes is considered in the thesis by Lau [31] that accounts for different angles of embrace. Neglecting hoop stresses, the minimum thrust to weight ratio for a hemispherical dome with t/R=0.2 is conservatively around 20%, see also [16]. Accounting for compression–only hoop forces, the thrust to weight ratio computed using the modified trust line method falls below 15%. Numerical simulations using the linear elastic masonry–like material model report $H/V = 16.6\%$, in good agreement with the above analytical investigations based on the Heyman's assumption. It must be remarked that in hemispherical domes hoop stresses provide a noticeable benefit in terms of thrust. In ogival domes they are essential to find a no–tension solution, see

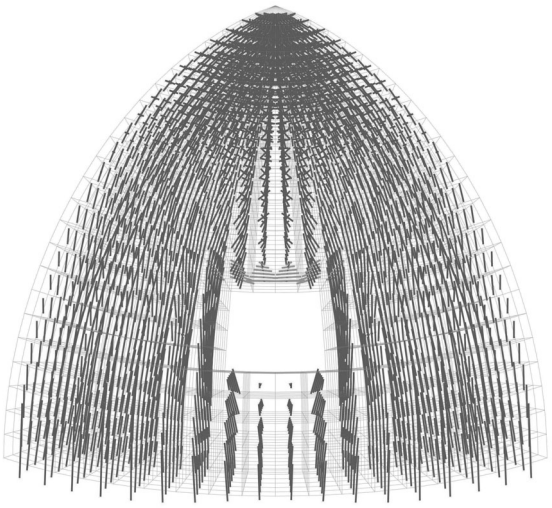

(a)

Figure 20: Example 3. Equilibrium of a cracked emispherical dome with openings under self weight: principal compressive stresses in the dome.

[44].

Any perturbation of geometry or loading makes it difficult to use the analytical method described above. This is the case of a dome endowed with symmetrical square holes underneath tensile–resisting lintels. Figure 20 shows the principal stresses of the compression–only solution found at convergence for this particular geometry. The lintel allows for a deviation of the meridional forces around the hole, inducing a noticeable modification of the stress fluxes also in the upper part of the dome. Minimum reactions are found below the opening, as expected. With respect to the original intact dome, maximum reactions increase to $V = 105.3$ kN/m and $H = 21.2$ kN/m, for a thrust to weight ratio $H/V = 20\%$.

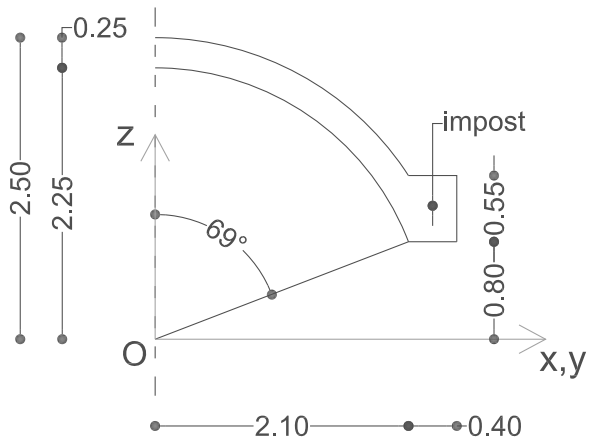

Figure 21: Example 4. Geometry of a groin vault. Dimensions in m.

4.4. Example 4. Load paths in a cracked groin vault

A groin vault with square plan is herein considered. Half of the typical section showing the impost is given in Figure 21. The vault is generated by the intersection of two perpendicular barrel vaults. Each of them is formed by the extrusion of a segmental arch, with span $S = 4.20$ m, rise $R_s = 1.45$ m and thickness $t = 0.25$ m. The linear elastic masonry–like material is that of the previous example. The cross vault is sustained at its four corners, assuming restraints on the vertical and horizontal displacements only at the height of the impost.

Funicular analysis has extensively been used to cope with the equilibrium of arcuate masonry vaults, see the pioneering work [43]. This technique models the principal stresses in a masonry vault as a discrete network of forces that is constrained to lie within the brickwork and be in equilibrium with the loads applied to the vault. In general, the plan projection of the network is assumed, whereas variable horizontal thrusts are used to adjust the funicular polygon handling the equilibrium. To define a suitable topology, different assumptions can be made referring to the expected flow of the principal stresses in the cracked regime. Figure 22 refers to the case of

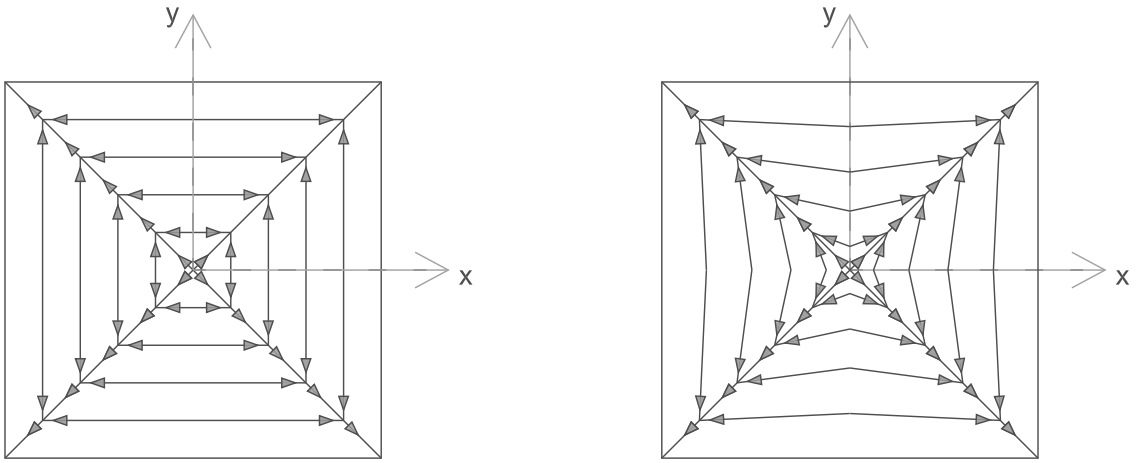

Figure 22: Example 4. Possible load paths for self weight only for a groined vault according to [43]. Representation in plan.

self–weight and shows two possible load paths proposed in [43], see also [10]. Both assume that distributed loads are conveyed by the four segments of the cross vault to the groins, such that the maximum thrusts arise at all four corner imposts and lie along the diagonals of the square plan. One can assume that loads are conveyed to the groins along paths that are parallel to the side of the vault's plan (left diagram), or with increasing inclination when approaching the center (right diagram). Both diagrams can be combined to generate a network's topology that is rich enough to approximate with reasonable accuracy the stress pattern that is expected in the cracked regime. It is worth remarking that the first diagram is in agreement with the statically admissible stress field derived in [5]. Moreover, it can be used to implement an extension of the thrust line method originally conceived for simple arches that can be handled analytically, see e.g. [17].

Load paths and principal stresses can alternatively be recovered resorting to the linear elastic masonry–like material model. A mesh of 2008 six–node and eight–node finite elements is used to model a quarter of the vault under self–weight (symmetry with respect to the segments' axes

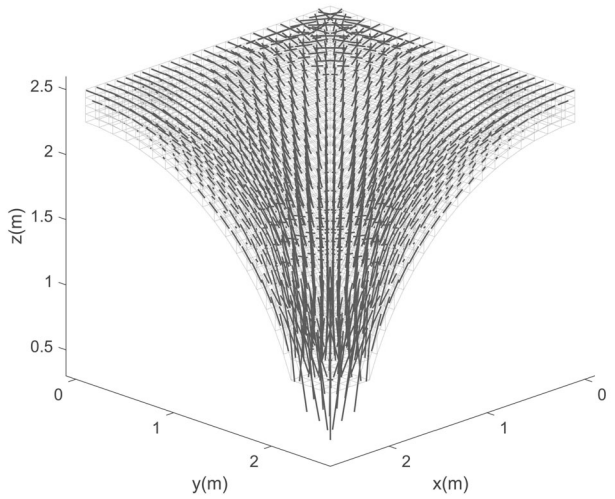

Figure 23: Example 4. Principal stresses in the vault under self weight.

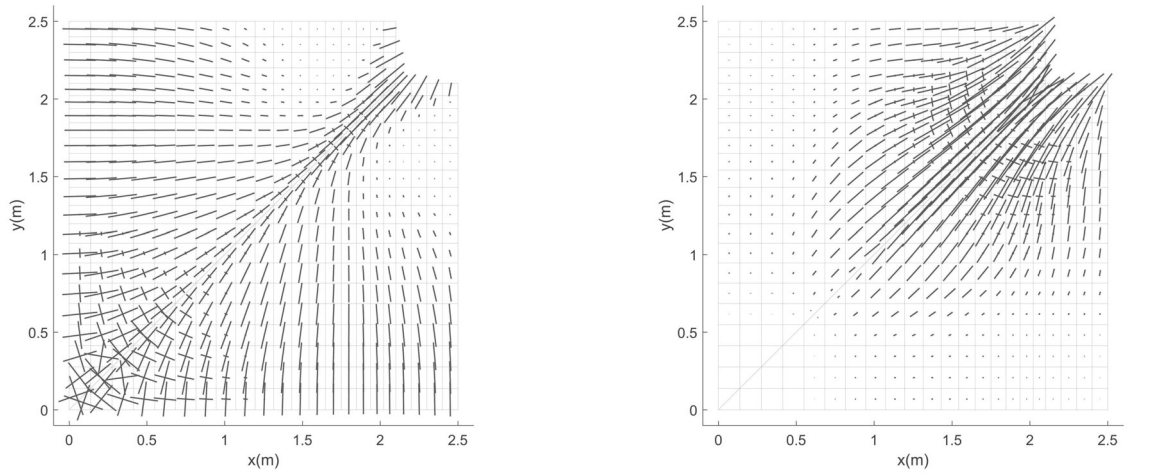

(a) (b)

Figure 24: Example 4. Principal stresses in the vault under self weight: extrados (a) and intrados (b).

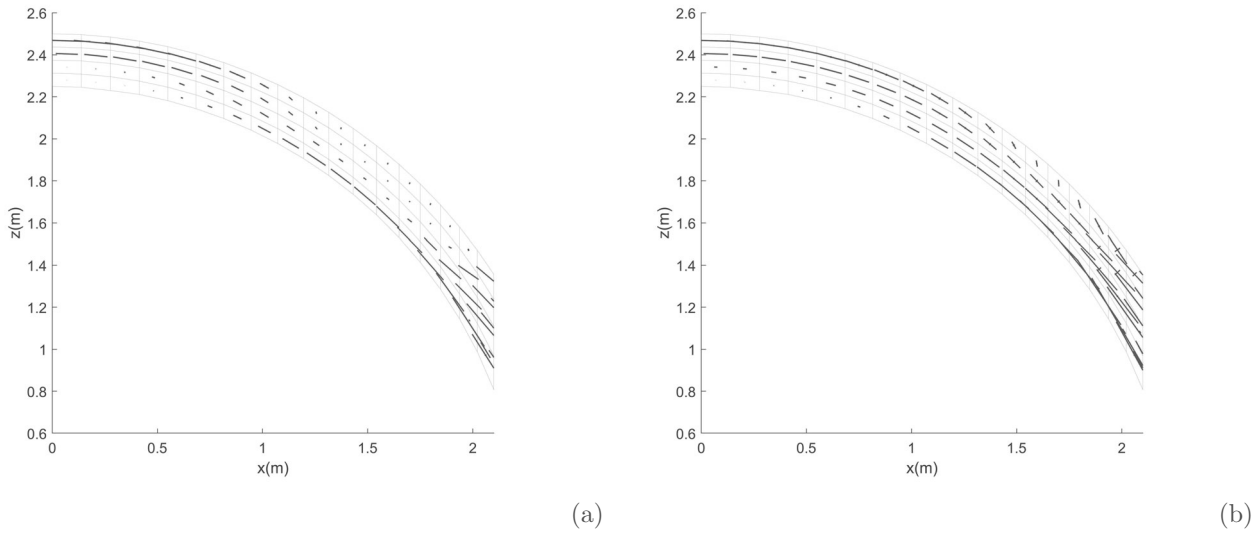

(a) (b)

Figure 25: Example 4. Principal stresses in a section of the vault at $y = 2.4$ m loaded by: self–weight (a) and self–weight and infill (b).

holds both for geometry and loads). The weight is applied as a surface pressure on the elements at the extrados of the vault, depending on γ_m and t. Displacements are fully restrained for all the nodes at $z = 0.80$ m. Figure 23 shows a three–dimensional view of the principal compressive stresses found at convergence by the proposed algorithm, whereas Figure 24(a) and (b) refer to the extrados and intrados, respectively.

Stress–free regions are found at the extrados (at the haunches of the vault segments) and, especially, at the intrados (around the crown of the segments): extended cracks are expected to arise there. A biaxial stress state is found in the central zone of the extrados. However, a significant portion of the vault undergoes an almost uniaxial compression: the crucial role of the groins conveying the diagonal thrust to the imposts is recovered, as expected. Uniaxial stresses flow parallel to the sides of the vault far from the center and the haunches, while steering towards

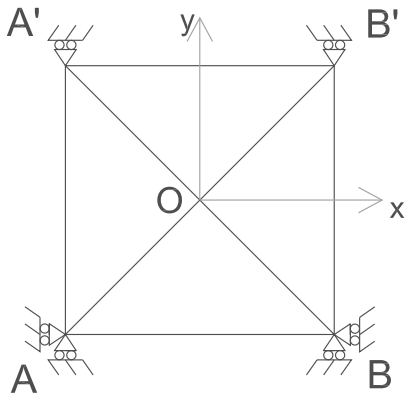

Figure 26: Example 4. In–plane boundary conditions to investigate the effect of lateral loads in case of stiff abutments at A B and compliant ones at A' B'.

the diagonals in those regions. Hence, features of both diagrams in Figure 22 can be recognized in the computed solution.

Figure 25 shows a vertical section of the vault at $y = 2.4$ m (parallel to the side of the vault, close to the boundary), comparing stresses computed when only self–weight is considered (a) to those found adding to it the weight of the infill. It is assumed that the infill reaches the height $z_i = 2.6$ m and its specific weight is $\gamma_i = 18$ kN/m^3. As expected, the vault benefits remarkably from this additional load. In the latter case, the resulting line of pressure is closer to the center of the section, thus allowing for a reduction of the extension of the cracked regions.

A final investigation is performed considering the seismic behaviour of the vault. It is assumed that the vault belongs to the side aisle of a church. Due to the remarkable difference in terms of lateral stiffness of the supporting elements (inner columns/external wall), an in–plane horizontal shear distortion is expected in case of an earthquake, see in particular [24]. Figure 26 shows in–plane boundary conditions that may be adopted to investigate this particular scenario: corners A and B abut a stiff wall, whereas corners A' and B' lean on more compliant columns.

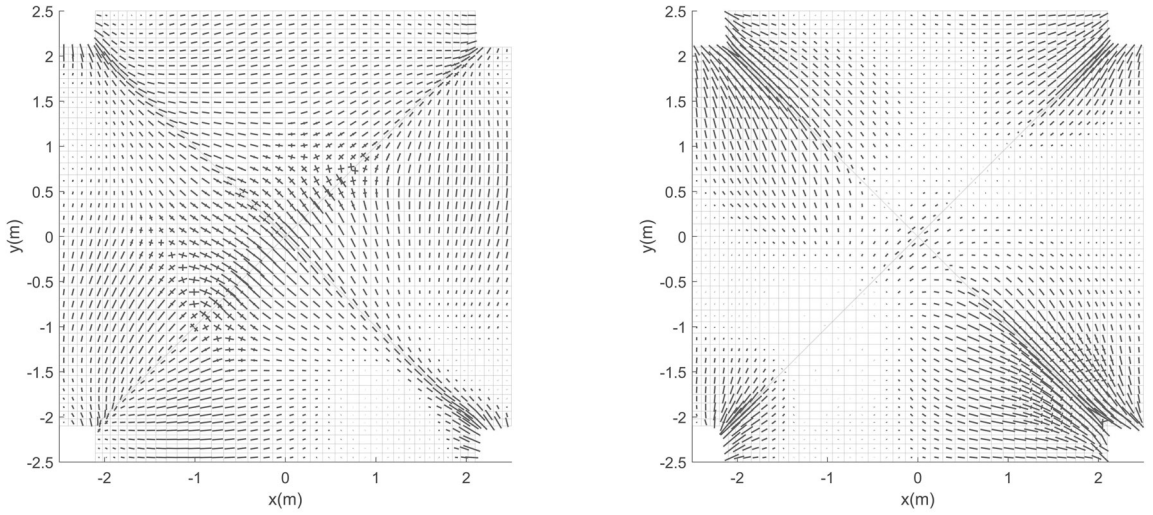

Figure 27: Example 4. Principal stresses in the vault under vertical and horizontal loads: extrados (a) and intrados (b).

Both transversal and longitudinal displacements are fully constrained in A and B, whereas only transversal displacements are fully restrained in A' and B'. Additionally, the (nonzero) longitudinal displacement in A' is forced to be the same as in B'.

A mesh of 8032 elements is used in the simulation. Rightward horizontal loads are added at the extrados for $x < 0$: they include 25% of the relevant structural weight and of the weight of the infill. Additional investigations could be performed combining horizontal components of the seismic force with a suitable vertical component, thus assessing the funicular equilibrium for any increase or decrease of the gravity loads.

Figure 27 shows the principal compressive stresses found at convergence by using the proposed algorithm, both at the extrados and at the intrados of the vault. Stress–free regions detect zones where noticeable (cracking) strains are expected.

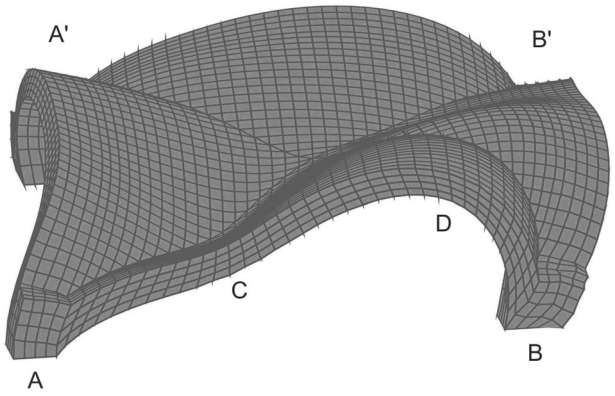

Figure 28: Example 4. Magnified deformed geometry of the vault under vertical and horizontal loads.

The extended numerical investigation performed in [24] suggests that groin vaults of similar geometry are likely to collapse under the applied shear distortion because of a four–hinge mechanism. Figure 28 shows the magnified deformed geometry that is in agreement with this outcome. Indeed, for increased values of the horizontal loads, the deformed geometry becomes a collapse mode with hinges *A*-*B*-*C*-*D*.

Finally, Figure 29 provides the history plots of the objective function for a quarter of the vault analyzed under vertical loads and compared to that of the simulation of the full domain subjected to vertical and horizontal loads. In both cases, less than 20 iterations are needed to solve equilibrium.

5. Conclusions and perspectives

A numerical approach has been presented to solve the equilibrium of three–dimensional linear elastic masonry–like structures exploiting the application programming interface of a general purpose software package that performs finite element analysis.

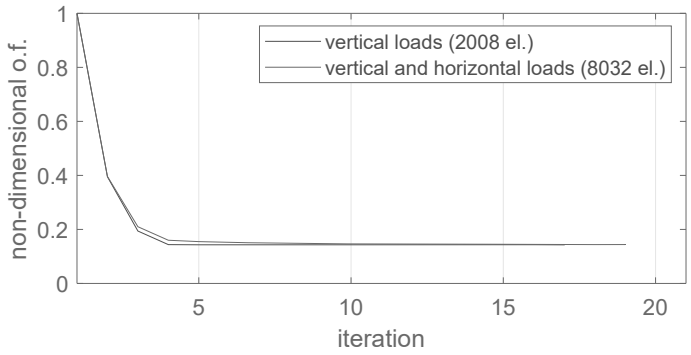

Figure 29: Example 4. History plot of the non–dimensional objective function: vertical loads with 2008 elements vs. vertical and horizontal loads with 8032 elements.

Masonry is replaced by an equivalent composite with spatially varying elastic properties and negligible stiffness in the case of cracking strains. The distribution of the equivalent orthotropic material is found by minimizing the strain energy to achieve a compression–only state of stress for any given compatible load. Instead of using mathematical programming, the minimization is performed by adopting a steepest descent–like update scheme that is driven by a set of penalized sensitivities. Little input and output data are exchanged between the main program and the finite element software package to run iteratively the analyses on the equivalent space–varying composite. The energy–based approach handles the equilibrium without accounting for the previous load history, as conversely required by incremental approaches. The implementation within a finite element package enables solids of general shape to be considered and exploits efficient sparse linear solvers.

Applications are shown referring to the preliminary assessment of structural components in historical masonry constructions. Indeed, the linear elastic no-tension material model is intended for monotonic loading and can not deal with sliding or crushing mechanisms. Also, the inelastic strain can not be used to predict crack patterns and crack widths. However, the adopted model calls

for the definition of a limited number of constitutive parameters and its numerical implementation is ideally conceived to visualize load paths both at the cracking state (see the hemispherical domes of Section 4.3 and the groin vault of Section 4.4) and at incipient collapse (see the wall in Section 4.2 subject to both vertical and horizontal loads). The proposed algorithm retrieves failure mechanisms that are in agreement with those found from limit load analysis, without requiring any *a–priori* assumption on the shape of the collapse mode or adopting any simplification in the geometry.

It has been shown that the proposed approach can predict horizontal thrusts at the base of cracked hemispherical domes that match those found through established methods available in the literature. Additionally, stresses can be evaluated at any point of the domain, regardless of the presence of peculiar geometrical features such as holes. Load paths found in cracked groin vaults are in agreement with those expected from the literature on the statics of architectural heritage. They can be used to assess the safety of the vault looking at the value of the stress peaks and at the extension of the cracked regions. Such kind of assessment can be performed under vertical loads, as self–weight and infill weight, or including also horizontal actions, such as for the in–plane shear test presented in Section 4.4. Alternatively, load paths can inspire refined network topologies to be used by numerical methods implementing funicular analysis.

Referring to the numerical features of the proposed algorithm, smooth history plots of the objective function result from the simulations. A limited number of iterations is generally required to achieve convergence.

The on–going research is mainly concerned with the analysis of structures made of layers exhibiting abrupt changes in terms of material properties, such as masonry vaults retrofitted with mortar or concrete layers. Moreover, an extension of the proposed energy–based approach to the optimal reinforcement of three–dimensional linear elastic no–tension structures is under investigation, see [14].

Acknowledgement

The authors gratefully acknowledge the financial support of Fondazione Cariplo through grant number 2017–0317 and Italian Ministry of Education University and Research through grant number 2015JW9NJT

References

[1] Alfano G, Rosati L, Valoroso N. A numerical strategy for finite element analysis of no-tension materials. Int J Numer Meth Eng 2000;48(3):317-350. https://dx.doi.org/10.1002/(SICI)1097-0207(20000530).

[2] Ananiev S. On equivalence between optimality criteria and projected gradient methods with application to topology optimization problem. Multibody Syst Dyn 2005;13(1):25-38. http://dx.doi.org/10.1007/s11044-005-2530-y.

[3] Angelillo M. Constitutive relations for no-tension materials. Mecc 1993;28(3):195-202. http://dx.doi.org/10.1007/BF00989121.

[4] Angelillo M, Cardamone L, Fortunato A. A Numerical model for masonry–like structures. J Mech Mater Struct 2010;5(4):583-615. http://dx.doi.org/10.2140/jomms.2010.5.583.

[5] Angelillo M, Babilio E, Fortunato A. Singular stress fields for masonry-like vaults. Continuum Mech Thermodyn 2013;25(2-4):423-441 http://dx.doi.org/10.1007/s00161-012-0270-9.

[6] Baratta A, Corbi O. An approach to masonry structural analysis by the no-tension assumption-Part I: material modeling, theoretical setup, and closed form solutions. Appl Mech Rev 2010;63(4): 040802. http://dx.doi.org/10.1115/1.4002790.

[7] Berke L, Khot NS. Structural Optimization Using Optimality Criteria. In: Mota Soares CA, editor. Computer Aided Optimal Design: Structural and Mechanical Systems, Berlin, Heidelberg: Springer;1987, p.271-211. http://dx.doi.org/10.1007/978-3-642-83051-8_7.

[8] Berto L, Saetta A, Scotta R, Vitaliani R. An orthotropic damage model for masonry structures. Int J Numer Meth Eng 2002;55(2):127-157. http://dx.doi.org/10.1002/nme.495.

[9] Billington DP. Thin shell concrete structures. New York:McGraw–Hill Book Company;1982.

[10] Block P, Lachauer L. Three–dimensional (3D) equilibrium analysis of gothic masonry vaults. Int J Archit Herit 2014;8(3):312-335 http://dx.doi.org/10.1080/15583058.2013.826301.

[11] Briccola D, Bruggi M, Taliercio A. Analysis of 3D no-tension masonry–like walls. In Angelillo M and Huerta Fernández S, Structural Analysis of Real Historic Buildings, J Mech Mater Struct, to appear

[12] Bruggi M. Finite element analysis of no–tension structures as a topology optimization problem. Struct Multidiscip Opt 2014;50(6):957-973. http://dx.doi.org/10.1007/s00158-014-1093-z.

[13] Bruggi M, Taliercio A. Analysis of no-tension structures under monotonic loading through an energy-based method. Comput Struct 2015;159:14-25. http://dx.doi.org/10.1016/j.compstruc.2015.07.002.

[14] Bruggi M, Taliercio A. Optimal strengthening of no-tension structures with externally bonded reinforcing layers or ties. Struct Mutltidiscip Opt 2017;55(5):1831-1846. http://dx.doi.org/10.1007/s00158-016-1625-9.

[15] Chisari C, Macorini L, Amadio C, Izzuddin BA. Identification of mesoscale model parameters for brick-masonry. Int J Solids Struct 2018;146:224-240. http://dx.doi.org/10.1016/j.ijsolstr.2018.04.003.

[16] Coccia S, Como M, Di Carlo F. Minimum thrust and minimum thickness of hemispherical masonry domes. Acta Mech 2016;227(9):2415-2425. http://dx.doi.org/10.1007/s00707-016-1630-5.

[17] Como M. Statics of Historic Masonry Constructions. Springer Series in Solid and Structural Mechanics. Heidelberg: Springer International Publishing;2017. http://dx.doi.org/10.1007/978-3-319-54738-1.

[18] Custódio AL, Madeira JFA. GLODS: Global and Local Optimization using Direct Search. J of Global Optim 2015;62(1). http://dx.doi.org/10.1007/s10898-014-0224-9.

[19] Cundall P. A Formulation of a three–dimensional distinct element model-Part I. A scheme to detect and represent contacts in a system composed of many polyhedral blocks. Int J Rock Mech Min Sci Geomech Abstr 1988;25(3):107-116. http://dx.doi.org/10.1016/0148-9062(88)92293-0.

[20] Cuomo M, Ventura G. A complementary energy formulation of no-tension masonry–like solids. Comput Methods Appl Mech Eng 2000;189(1):313-339. http://dx.doi.org/10.1016/S0045-7825(99)00298-4.

[21] D'Ayala D, Speranza E. Definition of collapse mechanisms and seismic vulnerability of historic masonry buildings. Earthq Spectra 2003;19(3):479-509. http://dx.doi.org/10.1193/1.1599896.

[22] Del Piero G. Constitutive equation and compatibility of the external loads for linear elastic masonry–like material. Mecc 1989;24(3):150-162. http://dx.doi.org/10.1007/BF01559418.

[23] Fraternali F. A thrust network approach to the equilibrium problem of unreinforced masonry vaults via polyhedral stress functions. Mech Res Commun 2010;37(2):198–204. http://dx.doi.org/10.1016/j.mechrescom.2009.12.010.

[24] Gaetani A, Lourenço PB, Monti G, Milani G. A parametric investigation on the seismic capacity of masonry cross vaults. Eng Struct 2017;148:686-703. http://dx.doi.org/10.1016/j.engstruct.2017.07.013.

[25] Genna, F. An accurate numerical integration scheme for solving structural problems in the presence of a "no-tension" materials. Comput Struct 1994;53(2):253-273. http://dx.doi.org/10.1016/0045-7949(94)90201-1.

[26] Grimaldi A, Sacco E. Energia Complementare e Metodo Penalty Per Problemi Elastici Unilaterali. Atti IX Congresso Nazionale AIMETA, Bari Ottobre 1988.

[27] Haftka R.T. Elements of Structural Optimization. Dordrecht: Kluwer Academic Publishers;1992.

[28] Heyman J. The stone skeleton. Int J Solids Struct 1966;2(2):249-279. http://dx.doi.org/10.1016/0020-7683(66)90018-7.

[29] Heyman J. Equilibrium of shell structures. Vol 6. Oxford: Oxford University Press;1977.

[30] Huerta S. Mechanics of masonry vaults: the equilibrium approach. In: Lourenço PB, Roca P, Proceedings of Historical Constructions, Guimar˜ães 47–69 2001.

[31] Lau W. Equilibrium Analysis of Masonry Domes. PhD Thesis. Massachusetts Institute of Technology 2006. http://dspace.mit.edu/bitstream/handle/1721.1/34984/71791712-MIT.pdf?sequence=2.

[32] Lemos JV. Discrete element modeling of masonry structures. Int J Archit Herit 2007;1(2):190-213. http://dx.doi.org/10.1080/15583050601176868.

[33] Livesley RK. Limit analysis of structures formed from rigid blocks. Int J Numer Meth Eng 1978;12(12):1853-1871. http://dx.doi.org/10.1002/nme.1620121207.

[34] Lourenço PB, De Borst R, Rots JG. A plane stress softening plasticity model for orthotropic materials. Int J Numer Meth Eng 1997;40(21):4033-4057. https://doi.org/10.1002/(SICI)1097-0207(19971115).

[35] Lourenço PB. Analysis of historical constructions: from thrust-lines to advanced simulations. Historical constructions 2001;91-116.

[36] Lucchesi M, Padovani C, Pasquinelli G. On the numerical solution of equilibrium problems for elastic solids with bounded tensile strength. Comput Methods Appl Mech Eng. 1995;127:37-56. http://dx.doi.org/10.1016/0045-7825(95)00816-4.

[37] Lucchesi M, Padovani C, Pasquinelli G, Zani N. Statics of masonry vaults, constitutive model

and numerical analysis. J Mechan Mater Struc 2007;2(2):221–244. http://dx.doi.org/10.2140/jomms.2007.2.221.

[38] Macorini L, Izzuddin BA. Nonlinear analysis of masonry structures using mesoscale partitioned modelling. Adv Eng Software 2013;60-61:58-69. http://dx.doi.org/10.1016/j.advengsoft.2012.11.008.

[39] Madeira JFA, Rodrigues H, Pina H. Multi-objective optimization of structures topology by genetic algorithms. Adv Eng Software 2005;36(1):21-28.. http://dx.doi.org/10.1016/j.advengsoft.2003.07.001.

[40] Maier G, Nappi A. A theory of no-tension discretized structural systems. Eng Struct 1990;12(4):227-234. http://dx.doi.org/10.1016/0141-0296(90)90021-J.

[41] Marfia S, Sacco E. Numerical procedure for elasto-plastic no-tension model. Int J Comp Meth-Sing 2005;6(3):187-199. http://dx.doi.org/10.1080/15502280590923739.

[42] Minga E, Macorini L, Izzuddin BA. Enhanced mesoscale partitioned modelling of heterogeneous masonry structures. Int J Numer Methods Eng 2018;113(13):1950-1971. http://dx.doi.org/10.1002/nme.5728.

[43] O'Dwyer D. Funicular analysis of masonry vaults. Computers and Structures 1999;73(1-5):187-197. http://dx.doi.org/10.1016/S0045-7949(98)00279-X.

[44] Oppenheim IJ, Gunaratnam DJ, Allen RH. Limit state analysis of masonry domes. J Struct Eng 1989;115(4):868-882. http://dx.doi.org/10.1061/(ASCE)0733-9445(1989)115:4(868).

[45] Pelà L, Cervera M, Roca P. Continuum damage model for orthotropic materials: Application to masonry. Comput Methods Appl Mech Eng 2011;200(9-12):917-930. http://dx.doi.org/10.1016/j.cma.2010.11.010.

[46] Roca P, Cervera M, Gariup G, Pelà L. Structural analysis of masonry historical constructions. Classical and advanced approaches. Arch Comput Meth Eng 2010;17(3):299-325. http://dx.doi.org/10.1007/s11831-010-9046-1.

[47] Sacco E. Modellazione e calcolo di strutture in materiale non resistente a trazione. Atti della Accademia Nazionale dei Lincei. Classe di Scienze Fisiche, Matematiche e Naturali. Rendiconti Lincei. Matematica e Applicazioni 1990;1(3):235-258. http://www.bdim.eu/item?id=RLIN_1990_9_1_3_235_0.

[48] Sacco E, Addessi D, Sab K. New trends in mechanics of masonry. Mecc 2018;53(7):1565-1569. http://dx.doi.org/10.1007/s11012-018-0839-x.

[49] Tralli A, Alessandri C, Milani G. Computational methods for masonry vaults: A review of recent results. Open Civ Eng J 2014;8(1):272-287. http://dx.doi.org/10.2174/1874149501408010272.

[50] Vannucci P. Anisotropic Elasticity. Lecture Notes in Applied and Computational Mechanics book series. Vol 85. Heidelberg: Springer International Publishing;2018. http://dx.doi.org/10.1007/978-981-10-5439-6.

[51] Zessin J, Lau W, Ochsendorf J. Equilibrium of cracked masonry domes. Proceedings of the Institution of Civil Engineers: Engineering and Computational Mechanics 2010;163(3):135-145. http://dx.doi.org/10.1680/eacm.2010.163.3.135.